MINISTÉRIO DA EDUCAÇÃO
Universidade Federal de Juiz de Fora
Faculdade de Engenharia
Programa de Pós-Graduação em Engenharia Civil

Victor Higino Meneguitte Alves

Structural Health Monitoring using Unsupervised Quantum Machine Learning

Juiz de Fora

2025

Victor Higino Meneguitte Alves

Structural Health Monitoring using Unsupervised Quantum Machine Learning

Dissertation presented to the Postgraduate Program in Civil Engineering at the Federal University of Juiz de Fora as part of the requirements for obtaining the title of Master's Degree in Civil Engineering.

Date of approval: 10/03/2025

Area of concentration: Structures and Materials

Research line: Structural Mechanics

Advisor: Prof. Dr. Alexandre Abrahão Cury – UFJF

Co-advisor: Prof. Dr. Raphael Fortes Infante Gomes – UNILA

Juiz de Fora

2025

Ficha catalográfica elaborada através do programa de geração
automática da Biblioteca Universitária da UFJF,
com os dados fornecidos pelo(a) autor(a)

Higino Meneguitte Alves, Victor.
Structural Health Monitoring using Unsupervised Quantum Machine Learning / Victor Higino Meneguitte Alves. -- 2025.
89 p.

Orientador: Alexandre Abrahão Cury
Coorientador: Raphael Fortes Infante Gomes
Dissertação (mestrado acadêmico) - Universidade Federal de Juiz de Fora, Faculdade de Engenharia. Programa de Pós-Graduação em Engenharia Civil, 2025.

1. structural health monitoring. 2. quantum machine learning. 3. damage detection. 4. quantum computing. 5. unsupervised learning. I. Abrahão Cury, Alexandre, orient. II. Fortes Infante Gomes, Raphael, coorient. III. Título.

PROGRAMA DE PÓS-GRADUAÇÃO EM ENGENHARIA CIVIL

Victor Higino Meneguitte Alves

Título: "Structural Health Monitoring using Unsupervised Quantum Machine Learning"

Dissertação apresentada ao Programa de Pós Graduação em Engenharia Civil da Universidade Federal de Juiz de Fora como requisito parcial à obtenção do título de Mestre em Engenharia Civil. Área de concentração: Estruturas e Materiais

Aprovada em 10/03/2025

BANCA EXAMINADORA

Prof. Dr. Alexandre Abrahão Cury - Orientador e Presidente da Banca
Universidade Federal de Juiz de Fora

Prof. Dr. Raphael Fortes Infante Gomes-Coorientador
Universidade Federal de Integração Latino-Americana

Prof. Dr. Celso Jorge Villas-Boas- Membro titular externo
Universidade Federal de São Carlos

Prof. Dr. Flávio de Souza Barbosa - Membro titular interno
Universidade Federal de Juiz de Fora

Juiz de Fora, 10/03/2025.

Documento assinado eletronicamente por **Alexandre Abrahao Cury**, **Professor(a)**, em 10/03/2025, às 18:18, conforme horário oficial de Brasília, com fundamento no § 3º do art. 4º do Decreto nº 10.543, de 13 de novembro de 2020.

Documento assinado eletronicamente por **RAPHAEL FORTES INFANTE GOMES**, **Usuário Externo**, em 12/03/2025, às 09:15, conforme horário oficial de Brasília, com fundamento no § 3º do art. 4º do Decreto nº 10.543, de 13 de novembro de 2020.

Documento assinado eletronicamente por **Celso Jorge Villas Boas**, **Usuário Externo**, em 12/03/2025, às 14:54, conforme horário oficial de Brasília, com fundamento no § 3º do art. 4º do Decreto nº 10.543, de 13 de novembro de 2020.

Documento assinado eletronicamente por **Flavio de Souza Barbosa**, **Professor(a)**, em 12/03/2025, às 17:33, conforme horário oficial de Brasília, com fundamento no § 3º do art. 4º do Decreto nº 10.543, de 13 de novembro de 2020.

A autenticidade deste documento pode ser conferida no Portal do SEI-Ufjf (www2.ufjf.br/SEI) através do ícone Conferência de Documentos, informando o código verificador **2284469** e o código CRC **4F66BC79**.

I dedicate this work to my parents.

Acknowledgments

I extend my heartfelt gratitude to my parents and siblings for their unconditional support, love, and trust, which formed the foundation upon which I built my academic journey.

To my family, my girlfriend, and my friends for their encouragement and companionship in both joyful and challenging times.

To my advisor, Alexandre Cury, who ventured into the world of scientific research with me from my early days in college. His guidance has led me with wisdom and patience. I am deeply grateful to have him as a mentor and friend along this path.

To my co-advisor, Raphael Gomes, for introducing me to the fascinating world of Quantum Computing with such care and dedication.

To all the professors of the basic cycle, the Faculty of Engineering, and the Graduate Program in Civil Engineering (PEC-UFJF) for the invaluable lessons shared.

I am also thankful to everyone in the Research Group on Data Science Applied to Engineering (CIDENG) for the immense learning opportunities and the chance to engage in science communication about artificial intelligence.

To the members of the Laboratory of Imaging and Signals (LIS) at UFJF.

To the funding agencies CAPES, FAPEMIG, and CNPq for their financial support.

Finally, I extend my gratitude to everyone who, in one way or another, contributed to this journey.

Thank you all.

"I think I can safely say that nobody really understands quantum mechanics"

— Richard P. Feynman

Resumo

O presente estudo apresenta uma nova abordagem utilizando Aprendizado de Máquina Quântico não supervisionado (QML, do inglês *Quantum Machine Learning*) para o Monitoramento da Integridade Estrutural (SHM, do inglês *Structural Health Monitoring*). A metodologia proposta envolve a extração de características a partir de sinais de aceleração brutos e sua codificação em estados quânticos para posterior análise em um classificador quântico. Ao treinar o modelo com cenários conhecidos de integridade, uma função de pontuação de anomalias é avaliada para identificar desvios do comportamento normal, com o objetivo de detectar possíveis anomalias estruturais. O *framework* é validado por meio de aplicações experimentais em uma estrutura de laboratório de dois andares e em uma ponte ferroviária em escala real, demonstrando resultados promissores na detecção, localização e quantificação de anomalias. Através de experimentações e análises numéricas, este estudo avança na fronteira da pesquisa em SHM, estabelecendo as bases para futuras explorações na interseção entre Computação Quântica e Engenharia Civil.

Palavras-chave: monitoramento de integridade estrutural; aprendizado de máquina quântico; detecção de danos; computação quântica; aprendizado não supervisionado.

Abstract

This study presents a novel approach using unsupervised Quantum Machine Learning (QML) for Structural Health Monitoring (SHM). The proposed methodology involves extracting features from raw acceleration signals and encoding them into quantum states for a subsequent analysis in a quantum classifier. By training the model with known intact scenarios, an anomaly score function is evaluated to identify deviations from normal behavior aiming to detect potential structural anomalies. The framework is validated through experimental applications on a two-story laboratory frame and on a real-scale railway bridge, demonstrating encouraging results in anomaly detection, localization, and quantification. Through experimentation and numerical analyses, this study advances on the edge of SHM research, laying the foundation for future exploration at the intersection of Quantum Computing and Civil Engineering.

keywords: structural health monitoring; quantum machine learning; damage detection; quantum computing; unsupervised learning.

List of Acronyms

ADAM	Adaptative Moment Estimation
AI	Artificial Intelligence
CNN	Convolutional Neural Network
CWT	Continuous Wavelet Transform
DCNN	Deep Convolutional Neural Networks
DL	Deep Learning
HOS	Higher Order Statistics
LSTM	Long Short-Term Memory
ML	Machine Learning
NISQ	Noisy Intermediate-Scale Quantum
PCA	Principal Component Analysis
PSA	Peak Spectral Acceleration
QCNN	Quantum Convolutional Neural Network
QML	Quantum Machine Learning
Q-SVM	Quantum Support Vector Machines
SCADA	Supervisory Control and Data Acquisition
SDD	Structural Damage Detection
SHM	Structural Health Monitoring
SVM	Support Vector Machine
VMD	Variational Mode Decomposition

Summary

1 General Introduction 1

1.1 Motivation 2

1.2 Objective 3

1.3 Specific Objectives 3

1.4 Text Structure 4

1.5 References 4

2 Brief Literature Review 6

2.1 References 9

3 Article – New Perspectives on Structural Health Monitoring using Unsupervised Quantum Machine Learning 11

4 Final Considerations 76

5 Published Works Related to the Topic 77

1 GENERAL INTRODUCTION

Engineering structures are frequently subject to changes in their dynamic properties due to various factors such as traffic, temperature, wind, damage, and others (Alves *et al.*, 2015). These causes can be characterized as long-term (progressive) changes, which affect the service life of structures (e.g., fatigue, corrosion, excessive deformations, etc.), inadequate maintenance or unforeseen loads during design. They may also include sudden changes, which are less likely to occur but cause greater and unexpected damage, such as earthquakes, storms or vehicle accidents. This gives rise to the concept of Structural Health Monitoring (SHM), a set of methods and devices used to assess the "health" of structures (Farrar; Worden, 2007).

Traditional SHM techniques depend on modal analysis, which identifies modal parameters, such as natural frequencies (Mekjavić; Damjanović, 2017), damping ratios (Curadelli *et al.*, 2008), and vibration modes (Salawu; Williams, 1995) (Moughty; Casas, 2017). Nevertheless, the modal identification implies a filtering process that may result in information loss, disguising minor structural changes potentially related to damage (Alves *et al.*, 2015). Furthermore, modal parameter-based approaches presume that structures remain inside the linear elastic domain even after being damaged, which is not always the case. For example, Morales *et al.* (2018) concluded that no clear relationship could be established between natural frequencies, temperature variations and damage in a simply supported beam tested in a laboratory, highlighting the limitations of conventional methods when faced with environmental influences.

In parallel, Machine Learning has radically transformed the way in which we interact and deal with data sets. This area of knowledge is present in a wide range of applications, such as the programming of robots' Artificial Intelligence (A.I.), genetic recombination algorithms and facial recognition software. The functioning of such systems is based on the analysis of large data sets, forcing algorithms and computational resources to operate under conditions close to their limits.

Recent approaches have explored artificial intelligence (AI) strategies to detect structural degradation. These tools include (but are not limited to) Artificial Neural Networks (ANNs), Decision Trees (DT), Support Vector Machines (SVMs) and Convolutional Neural Networks (CNNs) (Zinno *et al.*, 2022). SHM is thus treated as a time-series classification task; however, these methods are predominantly supervised, requiring labeled vibrational data from both intact

and damaged structures (which is often impractical (Alves; Cury, 2021)). In such cases, finite element models are usually employed (Mariniello *et al.*, 2021), which may introduce uncertainties and calibration challenges. As a result, these methods also fail to identify unknown and/or untrained behaviors.

In general, data processing and exchange can be modeled through concepts associated with Classical Information Theory. However, with the progressive miniaturization of technology, quantum phenomena assume an increasing role in the scales of information processing technology present in current devices, in contrast to the effects generally described by Classical Physics. As a result, translating existing models, solution designs and approaches to Quantum Computing is a complex and non-trivial task, whose applications have aroused the interest of research areas and industrial sectors such as aerospace, agriculture, automotive, chemicals, energy, finance, government, healthcare, manufacturing, supply chain and telecommunications (Yndurain, 2025).

Under such conditions, the interface between Quantum Physics and Machine Learning generates two promising scenarios: if on the one hand it is estimated that Machine Learning algorithms can be applied in the understanding and control of quantum systems, on the other there is the expectation that quantum computing devices improve the performance of Machine Learning algorithms to solve problems that today are beyond the threshold of contemporary machines.

1.1 Motivation

This dissertation is justified by the need to overcome the limitations of traditional monitoring techniques, such as visual inspection and modal parameter analysis for detecting structural damage. Considering the innovation environment brought about by Industry 4.0, there is a growing demand for automated and scalable predictive maintenance approaches. While extensive literature explores AI applications in this context, few studies investigate the potential of Quantum Machine Learning (QML) for this purpose. Quantum algorithms possess unique capabilities to process large datasets and identify complex patterns, possibly enabling more accurate detection and localization of structural anomalies compared to classical approaches. As quantum hardware technology advances, these algorithms are expected to become more sophisticated and optimized, eventually surpassing classical learning methods in various applications.

Additionally, AI approaches are predominantly supervised, requiring categorized training data for both intact and damaged structures — a requirement that is often unfeasible due to the difficulty of obtaining comprehensive and representative datasets of real damage structures. Therefore, exploring unsupervised methods is important to overcome these limitations and provide more practical and technically feasible solutions.

1.2 Objective

The main objective of this dissertation is to investigate and evaluate the effectiveness of unsupervised QML algorithms for vibration-based SHM. The aim is to develop and test a methodology to autonomously detect damage in engineering structures using raw dynamic responses (e.g., acceleration signals). To the best of the author's knowledge, this represents the first application of an unsupervised quantum algorithm for such purposes. Figure 1 illustrates the scope of this dissertation.

Figure 1 - Research fields related to the present dissertation

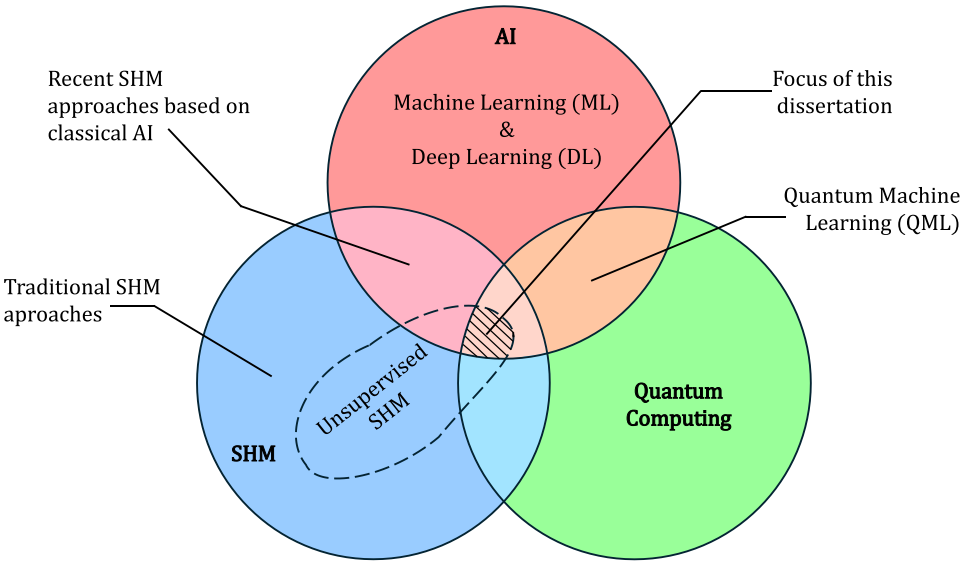

Source: The author

1.3 Specific Objectives

1. Develop a methodology for feature extraction from raw acceleration signals, encoding these signals into quantum states, and utilizing a quantum classifier for analysis.
2. Assess the performance of the proposed method in terms of damage detection, localization, and quantification.

3. Compare the effectiveness of the QML methodology with classical unsupervised machine learning methods, specifically: k-means clustering and hierarchical clustering.
4. Analyze the robustness of the proposed methodology regarding environmental variations, such as wind and temperature, particularly in real-scale structures.
5. Serve as a preliminary investigation that lays the groundwork for future explorations and innovations at the intersection of Quantum Computing and Civil Engineering.

1.4 Text Structure

The dissertation is organized as follows: the general introduction presents the research topic and objectives. Chapter 2 reviews recent literature related to the subject, while Chapter 3 contains the paper accepted for publication in the journal Mechanical Systems and Signal Processing entitled “New Perspectives on Structural Health Monitoring using Unsupervised Quantum Machine Learning”. Finally, Chapter 4 presents concluding remarks and recommendations for future research.

1.5 References

ALVES, Vinicius.; CURY, Alexandre.; ROITMAN, Ney.; MAGLUTA, Carlos.; CREMONA, Christian. Structural modification assessment using supervised learning methods applied to vibration data. **Engineering Structures**, v.99, p. 439–448, 2015. DOI: 10.1016/j.engstruct.2015.05.003.

ALVES, Victor; CURY, Alexandre. A fast and efficient feature extraction methodology for structural damage localization based on raw acceleration measurements. **Structural Control and Health Monitoring**, v. 28, n. 7, p. e2748, 2021. DOI: 10.1002/stc.2748.

CURADELLI, R. O.; RIERA, J. D.; AMBROSINI, D.; AMANI, M. G. Damage detection by means of structural damping identification. **Engineering Structures**, v. 30, n. 12, p. 3497-3504, 2008. DOI: 10.1016/j.engstruct.2008.05.024.

FARRAR, Charles; WORDEN, Keith. An introduction to structural health monitoring. **Philosophical Transactions of the Royal Society A: Mathematical, Physical and Engineering Sciences**, v. 365, n. 1851, p. 303-315, 2007. DOI: 10.1098/rsta.2006.1928.

MARINIELLO, Giulio.; PASTORE, Tommaso.; MENNA, Costantino.; FESTA, Paola.; ASPRONE, Domenico. Structural damage detection and localization using decision tree

ensemble and vibration data. **Computer-Aided Civil and Infrastructure Engineering**, v. 36, n. 9, p. 1129-1149, 2021. DOI: 10.1111/mice.12633.

MEKJAVIĆ, Ivana; DAMJANOVIĆ, Domagoj. Damage assessment in bridges based on measured natural frequencies. **International Journal of Structural Stability and Dynamics**, v. 17, n. 02, p. 1750022, 2017. DOI: 10.1142/S0219455417500225.

MORALES, Fabricio A. O.; CURY, Alexandre A. Analysis of thermal and damage effects over structural modal parameters. **Structural engineering and mechanics: An international journal**, v. 65, n. 1, p. 43-51, 2018. DOI: 10.12989/sem.2018.65.1.043.

MOUGHTY, John J.; CASAS, Joan R. A state-of-the-art review of modal-based damage detection in bridges: Development, challenges, and solutions. **Applied Sciences**, v. 7, n. 5, p. 510, 2017. DOI: 10.3390/app7050510.

SALAWU, Olusegun S.; WILLIAMS, Clive. Bridge assessment using forced-vibration testing. **Journal of structural engineering**, v. 121, n. 2, p. 161-173, 1995. DOI: 10.1061/(asce)0733-9445(1995)121:2(161).

ZINNO, Raffaele; HAGHSHENAS, Sina; GUIDO, Giuseppe; VITALE, Alessandro. Artificial intelligence and structural health monitoring of bridges: A review of the state-of-the-art. **IEEE Access**, v. 10, p. 88058-88078, 2022. DOI: 10.1109/ACCESS.2022.3199443.

YNDURAIN, Elena. (2025). Quantum Computing Strategy: Foundations and Applicability. Chapman and Hall/CRC, USA. DOI: 10.1201/9781003302674.

2 BRIEF LITERATURE REVIEW

Estimating the current safety conditions of a specific structure is critical to ensure its performance throughout its service life. However, this prediction is strongly influenced by various factors such as environmental conditions, usage loads, design specifications and many other elements, resulting in complex interactions that often make comprehensive analysis impractical. Traditionally, structural assessment has been performed through human visual inspections, which can be impractical in remote locations and, furthermore, is subjective, relying on the engineer or technician's expertise. Visual inspections are also limited to the structure's surface and may fail to detect internal damage.

Structural Health Monitoring (SHM) systems have thus gained considerable interest among researchers across various fields, including Civil Engineering (Rabi *et al.*, 2024), Railway Engineering (Magalhães *et al*., 2024), Mechanical Engineering (Dreher *et al.*, 2023), Aerospace Engineering (Kosova *et al.*, 2025) and oil and gas industry (Wang et al., 2024). This interest stems from their non-destructive and real-time approach, which has the potential to reduce maintenance costs by optimizing repair frequency. Consequently, in the Industry 4.0 environment, predictive maintenance complements the preventive one.

In contrast, vibration-based structural integrity analysis involves assessing structures using dynamic data acquired from sensors mounted directly on the structure. This methodology is the primary focus of this research especially when combined with AI techniques, as it proves highly valuable in scenarios where visual inspection of structural issues becomes challenging or unfeasible.

In vibration-based SHM, the fundamental framework is the paradigm of structural damage identification, which consists of four levels according to Rytter (1993): detection (Level I), localization (Level II), quantification (Level III), and prognosis (Level IV). This research focuses on verifying the existence of damage (SHM Level I) and locating it (SHM Level II), fundamental aspects of ensuring structural safety. Additionally, the study investigates its validity for damage quantification (SHM Level III). Furthermore, the proposed anomaly index can be spatially visualized along the structure, facilitating analysis and decision-making for the responsible engineer during the prognosis stage (SHM Level IV).

In recent decades, advancements in Data Science and Machine Learning (ML) have made signal processing an ever-growing field and a crucial tool for SHM technologies (Avci et al.,

2021). In these vibration-based approaches, accelerometers are used to identify structural anomalies. In this context, Finotti et al. (2019) introduced a methodology for detecting structural changes based on statistical indicators and classification techniques, including ANN and SVM. Ten statistical indicators were extracted from vibrational data and used as inputs for classification methods. The methodology's effectiveness was evaluated through applications in three different scenarios: a numerical model of a simply supported beam subjected to various damage levels, a laboratory-manufactured steel beam and a railway bridge in France.

To advance to SHM Level II (damage localization), Alves and Cury (2021) employed data science and statistical techniques. Features in multiple domains (time, frequency, and quefrency) were extracted from vibration data of the structure in its reference (intact) state and current (unknown) state. The methodology involved creating an index that accurately represented the damage location(s) after extracting 35 handcrafted features from raw measurement data. Confidence intervals were established for each feature associated with the intact state, and unknown state properties were compared to these intervals, identifying damage accordingly.

More recent approaches have applied Deep Learning (DL) to structural degradation detection, addressing the challenge of time-series classification (Sony et al., 2022). Convolutional Neural Networks are the most common technique in this context for handling large volumes of raw data, and are the leading approach for pattern recognition in images (Cireșan et al., 2010). This strategy automatically extracts damage-sensitive information from acceleration signals training successive layers of neurons, in contrast to other data mining methods requiring manual feature creation. However, most DL approaches are supervised and may not effectively detect previously untrained behaviors.

Chegeni et al. (2022) proposed a feature extraction process based on coefficients and residues of autoregressive (AR) models to localize and quantify simple and multiple damages, and the study presented superior results compared to classical techniques. Additionally, there has been a recent increase in developing hybrid architectures combining various strategies to enhance SHM methodologies' effectiveness.

In the research conducted by Luleci, Catbas, and Avci (2023a), an alternative approach was developed to handle the large volume of training data. The authors used One-Dimensional Wasserstein Deep Convolutional Generative Adversarial Networks with Gradient Penalty (1-D

WDCGAN-GP) to generate supplementary synthetic dynamic signals representing the structure's damaged scenario. In other words, anomalous vibrational responses were created that were not experimentally collected. This methodology relies on two neural networks: a generator that produces vibrational data and a discriminator that estimates the authenticity of these signals. As learning progresses, the generator produces replicas nearly indistinguishable from the original data. The researchers validated the datasets generated using quantitative and qualitative approaches.

In a more recent development, Luleci, Catbas, and Avci (2023b) adopted an innovative GAN model variant, the One-Dimensional CycleWDCGAN-GP. This model not only learns to generate similar signal examples within the same context but also excels in understanding the complex relationship between two distinct data contexts: the intact and damaged states. The method's remarkable capability lies in capturing normal structure signals and transforming them into anomalous responses representing damage, effectively bridging the gap between the two data contexts. Although time-domain tests revealed notable performance, improvements in frequency-domain analyses are possible with more diverse training. This proposal used dynamic signals from a steel structure, including datasets representing damaged (loose bolt) and "healthy" structures, where data were used to train the CycleGAN model. Later, intact state signals were transformed into the damaged context and vice versa. Evaluation criteria ensured that results in both contexts closely resemble real data, corroborating the model's effectiveness in translating information between domains.

Despite its potential, QML's application in data-driven vibration SHM is limited. Current methods often overlook environmental and operational conditions, rely on simplistic models and use supervised frameworks that struggle with obtaining damaged samples. More robust, adaptable approaches are needed to handle real-world complexities. To date, no work has evaluated an unsupervised QML method for vibration-based SHM problems.

This dissertation introduces a novel strategy for using quantum circuits in unsupervised clustering for vibration-based SHM. It validates this approach with experimental and real-scale structures, addressing anomaly detection, localization, and quantification. The study compares the performance of quantum-enhanced methodology with classical clustering, highlighting the benefits and limitations of each one. By combining experimentation and numerical analysis, it

advances SHM research at the intersection of Quantum Computing and Civil Engineering through both laboratory and full-scale experiments.

2.1 References

ALVES, Victor; CURY, Alexandre. A fast and efficient feature extraction methodology for structural damage localization based on raw acceleration measurements. **Structural Control and Health Monitoring**, v. 28, n. 7, p. e2748, 2021. DOI: 10.1002/stc.2748.

AVCI, Onur; ABDELJABER, Osama; KIRANYAZ, Serkan; HUSSEIN, Mohammed; GABBOUJ, Moncef; INMAN, Daniel. A review of vibration-based damage detection in civil structures: From traditional methods to Machine Learning and Deep Learning applications. **Mechanical systems and signal processing**, v. 147, p. 107077, 2021. DOI: 10.1016/j.ymssp.2020.107077.

CHEGENI, Masoud; SHARBATDAR, Mohammad; MAHJOUB, Reza; RAFTARI, Mahdi. New supervised learning classifiers for structural damage diagnosis using time series features from a new feature extraction technique. **Earthquake Engineering and Engineering Vibration**, v. 21, n. 1, p. 169-191, 2022. DOI: 10.1007/s11803-022-2079-2.

CIREŞAN, Dan; MEIER, Ueli; GAMBARDELLA, Luca; SCHMIDHUBER, Jürgen. Deep, big, simple neural nets for handwritten digit recognition. **Neural Computation**, v. 22, n. 12, p. 3207-3220, 2010. DOI: 10.1162/NECO_a_00052.

DREHER, Nathali Rolon; STORTI, Gustavo Chaves; MACHADO, Tiago Henrique. Vibration Signal Evaluation Based on K-Means Clustering as a Pre-Stage of Operational Modal Analysis for Structural Health Monitoring of Rotating Machines. **Energies**, v. 16, n. 23, p. 7848, 2023. DOI: 10.3390/en16237848.

FINOTTI, Rafaelle Piazzaroli; CURY, Alexandre Abrahão; BARBOSA, Flávio de Souza. An SHM approach using machine learning and statistical indicators extracted from raw dynamic measurements. **Latin American Journal of Solids and Structures**, v. 16, 2019. DOI: 10.1590/1679-78254942.

KOSOVA, Furkan; ALTAY, Özkan; ÜNVER, Hakkı Özgür. Structural health monitoring in aviation: a comprehensive review and future directions for machine learning. **Nondestructive testing and evaluation**, v. 40, n. 1, p. 1-60, 2025. DOI: 10.1080/10589759.2024.2350575.

LULECI, Furkan; CATBAS, F. Necati; AVCI, Onur. Generative adversarial networks for labeled acceleration data augmentation for structural damage detection. **Journal of Civil Structural Health Monitoring**, v. 13, n. 1, p. 181-198, 2023a. DOI: 10.1007/s13349-022-00627-8.

LULECI, Furkan; CATBAS, F. Necati; AVCI, Onur. CycleGAN for undamaged-to-damaged domain translation for structural health monitoring and damage detection. **Mechanical Systems and Signal Processing**, v. 197, p. 110370, 2023b. DOI: 10.1016/j.ymssp.2023.110370.

MAGALHÃES, Jorge; JORGE, Tomás; SILVA, Rúbens; GUEDES, António; RIBEIRO, Diogo; MEIXEDO, Andreia; MOSLEH, Araliya; VALE, Cecília; MONTENEGRO, Pedro; CURY, Alexandre A strategy for out-of-roundness damage wheels identification in railway vehicles based on sparse autoencoders. **Railway Engineering Science**, p. 1-23, 2024. DOI: 10.1007/s40534-024-00338-4.

RABI, Raihan Rahmat; VAILATI, Marco; MONTI, Giorgio. Effectiveness of Vibration-Based Techniques for Damage Localization and Lifetime Prediction in Structural Health Monitoring of Bridges: A Comprehensive Review. **Buildings**, v. 14, n. 4, p. 1183, 2024. DOI: 10.3390/buildings14041183.

RYTTER, Anders. **Vibrational based inspection of civil engineering structures**. 1993. Thesis (Doctorate in Civil Engineering) – Dept. of Building Technology and Structural Engineering, Aalborg University, Aalborg, 1993.

SONY, Sandeep; GAMAGE, Sunanda; SADHU, Ayan; SAMARABANDU, Jagath. Vibration-based multiclass damage detection and localization using long short-term memory networks. **Structures**, v. 35, p. 436-451, 2022. DOI: 10.1016/j.istruc.2021.10.088.

WANG, Yihuan; ZHU, Shiyi; WANG, Bohong; QIN, Jianjun; QIN, Guojin. Structural health monitoring of oil and gas pipelines: Developments, applications and future directions. **Ocean Engineering**, v. 308, p. 118293, 2024. DOI: 10.1016/j.oceaneng.2024.118293.

3 ARTICLE – NEW PERSPECTIVES ON STRUCTURAL HEALTH MONITORING USING UNSUPERVISED QUANTUM MACHINE LEARNING

Article published in the scientific journal: Mechanical Systems and Signal Processing (IF: 7.9).

- Victor Higino Meneguitte Alves, M.Sc. in Civil Engineering

  Graduate Program in Civil Engineering, Faculty of Engineering, University of Juiz de Fora, Juiz de Fora, Minas Gerais, Brazil.

- Raphael Fortes Infante Gomes, Assistant Professor

  Federal University of Latin American Integration, Foz do Iguaçu, Paraná, Brazil.

- Alexandre Abrahão Cury, Associate Professor

  Graduate Program in Civil Engineering, Faculty of Engineering, University of Juiz de Fora, Juiz de Fora, Minas Gerais, Brazil.

Abstract

This study presents a novel approach using unsupervised Quantum Machine Learning (QML) for Structural Health Monitoring (SHM). The proposed methodology involves extracting features from raw acceleration signals and encoding them into quantum states for a subsequent analysis in a quantum classifier. By training the model with known intact scenarios, an anomaly score function is evaluated to identify deviations from normal behavior aiming to detect potential structural anomalies. The framework is validated through experimental applications on a two-story laboratory frame and on a real-scale railway bridge, demonstrating encouraging results in anomaly detection, localization, and quantification. Through experimentation and numerical analyses, this study advances on the edge of SHM research, laying the foundation for future exploration at the intersection of Quantum Computing and Civil Engineering.

Keywords: Structural Health Monitoring. Quantum Machine Learning. Damage detection. Quantum Computing. Unsupervised learning.

1) Introduction

1.1) Background on SHM

Civil structures deteriorate over time due to continuous use and operational variables. Typically, large systems experience ongoing transformations in their characteristics due to a range of factors, which can be split into two main groups based on their duration. Firstly, there are long-lasting or progressive changes that have an impact on the structure's overall lifespan. Examples include fatigue, corrosion, abrasion, alkali–silica reaction, unanticipated loads during the design phase, among others [1]. Secondly, there are sudden changes that are less frequent but have potential to cause significant and unforeseen damage. This group includes events like earthquakes, storms, vehicle accidents, fires, floods and so on [2].

For this reason, methods and procedures for inspecting structures have been created to prevent both human fatalities and financial losses caused by abrupt or sustained damage, such as visual inspection and nondestructive testing. However, conventional inspection procedures like these often exhibit drawbacks, which include significant costs, time-consuming processes and potential risks to technicians and engineers. As a result, there has been a growing will to develop and implement Structural Health Monitoring (SHM) methods that can overcome these limitations and provide more autonomous, cost-effective, and safer alternatives for assessing structural integrity.

The paradigm of Structural Damage Detection (SDD) has been a constant pursuit. To standardize this process, researchers and practitioners have turned to Rytter's four-level scale [3] as a guiding framework. This scale has served as a compass, grouping SHM techniques based on their potential to address key questions at distinct levels of damage identification. From the foundation to the top, Level 1 corresponds to detecting the existence of damage within the structural system, Level 2 involves determining the exact location of the damage, and Level 3 focuses on assessing the severity or extent of the damage. Lastly, Level 4 encompasses the stage of evaluating the remaining lifespan or prognosis of the structure. Together, these levels form an organized framework that supports the SDD community, providing them with a powerful tool to manage the complexities of damage identification.

In parallel, vibration-based monitoring uses dynamic data acquired from sensors mounted in the structures to evaluate their integrity. This approach proves itself highly beneficial in situations when identifying structural issues solely through visual inspections is challenging or not feasible. For instance, anomalies or deterioration mechanisms can manifest within structural elements hidden from surface observation. The internal damage may include non-linearities, discontinuities, cracks, or voids inside the concrete [4,5]; hidden defects (such as corrosion of the embedded reinforcement), as well as broken fibers or delamination fractures in composite materials [6]. Hence, neglecting to recognize these issues poses significant safety risks. [7].

Finally, when discussing the challenges and limitations of vibration-based SHM, it is important to highlight the following topics: (a) Number of sensors: the effectiveness of the vibration-based approach is highly dependent on the quantity of sensors forming an adequate mesh. (b) Strategic sensors' location: it is crucial to plan a sensor network that accurately captures the dynamic characteristics of the structure, since achieving optimal sensor placement ensures the most useful information at the lowest possible cost [8]. (c) Environmental conditions: structures are exposed to various ambient factors that can affect the accuracy of vibration-based SHM methods due to noise and interference sources, which include wind velocity, traffic vibrations, temperature fluctuations, humidity, and so on. To ensure robust and accurate results, the techniques employed in each workflow should be capable of mitigating the impact of environmental noise and maintaining the integrity of the vibration measurements.

1.2) Recent related work

Over the past decades, the field of signal processing has witnessed significant growth and become a crucial component of SHM technologies, thanks to the advancements in Machine Learning (ML) and Deep Learning (DL) techniques [9, 10]. In the ML context, Bisheh and Amiri (2023) [11] introduced a method for structural damage detection using Variational Mode Decomposition (VMD) to extract time-frequency domain features from vibration response data, which were then applied with the Kernel Principal Component Analysis (KPCA) to reduce the feature matrix's dimensionality and mitigate environmental changes. In this scenario, a trained Support Vector Machine (SVM) was able to successfully discriminate between healthy and damaged states in numerical and full-scale cases.

As for DL-based methods, Chen et al. (2021)[12] presented a data-driven approach for damage detection utilizing the Continuous Wavelet Transform (CWT) combined with Deep Convolutional Neural Networks (DCNN). Their method was tested on two standard benchmarks references: the Qatar University Grandstand Simulator (QUGS) - for detecting damage in structural joints [13] - and the frame dataset from Los Alamos National Laboratory [14]. The results showed superior performance compared to existing ML methods such as SVM, CWT-SVM and random forest (RF). One year later, Sony et al. (2022) [15] developed a DL framework employing Long Short-Term Memory (LSTM) layers, which produced superior damage localization results compared to a CNN counterpart by using the first laboratory (QUGS).

Civera *et al.* (2022) [16] introduced and validated a multi-stage clustering algorithm for automatic operational modal analysis (AOMA) applied to unsupervised SHM. The method was experimentally tested on a scaled 1:2 model, which was progressively damaged to replicate foundation scouring at the central pier. The algorithm proved effective in identifying vibrational modes, damage detection and severity assessment. Showcasing its potential for fault detection in masonry structures, especially arch bridges. Furthermore, the study revealed that using traditional k-means clustering to select physical modes may be overly conservative when dealing with signals characterized by high noise levels or non-linear distortions.

Martucci *et al.* (2023) [17] explored the use of the Extreme Function Theory (EFT) in conjunction with Gaussian Process Regression (GPR) for damage detection SHM of bridges. The technique was experimentally applied to the I-40 bridge, demonstrating its ability to identify deviations from undamaged conditions using raw mode shapes, without the need for additional processing steps like deriving modal curvatures or using multiple modal parameters. Four degrees of damage were produced to replicate fatigue cracking via torch cuts in the web and flange. The results showed that the EFT framework exhibited high sensitivity to even small damages in the bridge's plate girders, outperforming traditional Extreme Value Theory (EVT) methods that rely on natural frequencies.

Regarding vision-based approaches, Zhang et al. (2021) [18] proposed a one-dimensional CNN-LSTM fracture detection technique for concrete bridge decks. In terms of precision and computation efficiency, their method outperformed current deep learning techniques for real-time crack identification. In turn, the work of Zhao et al. (2022) [19] maps

damage localization in a real concrete dam from unmanned aerial vehicle (UAV) images using an improved version of YOLOv5s architecture network and a 3D photogrammetric reconstruction method. Remarkably, the latter was able to identify large and small damage in real time without sacrificing their respective accuracies. However, when dealing with unseen concrete dams, this method presents a limitation regarding the need to increase the training dataset, which is a recurring disadvantage of supervised approaches.

More recently, a new research field with promising algorithms based on the main principles of Quantum Mechanics emerged: the Quantum Machine Learning (QML) [20]. In this context, the potential power of QML and the advantages of CNN led to the creation of novel techniques as the Quantum CNN (QCNN) [21]. Since then, some researchers assessed this approach working with different types of data: while Arthur (2022) [22] explores the potential of a hybrid-QCNN architecture using variational quantum circuits on many binary classification datasets, Yang et al. (2021)[23] investigate the use of QNN for speech recognition tasks. In turn, Wei et al. (2022) [24] employ QCNN for handwritten number recognition.

However, few studies addressed QML for SHM purposes. On the one hand, Trochun et al. (2021) [25] introduced a hybrid-QCNN designed for binary image classification to identify damaged buildings from satellite images. Nonetheless, the results showed slightly lower accuracies comparable to traditional models, emphasizing that the direct comparison of metrics between the best classical and hybrid classic-quantum algorithms might be premature in the initial stages in this field. On the other hand, the research of Correa-Jullian et al (2022) [26] explores the use of quantum kernel classification models, specifically the Quantum Support Vector Machines (Q-SVMs) for fault detection in wind turbine systems (WTSs). The data acquired by SCADA sensor measurements focused on early detection of pitch fault failures, and the methodology incorporated feature reduction techniques, such as Principal Component Analysis (PCA) and autoencoders (AE). The findings indicated that the quantum approach performs considerably well compared to conventional ML models (and sometimes can even outperform the last). In turn, the work of Bhatta and Dang (2024a) [27] was the first to use QCNN to identify damage in reinforced concrete (RC) buildings into multiple categories, whose approach is based on images taken after earthquakes. These results also confirmed that the seismic damage detection accuracy of this model is comparable to other CNN architectures.

Bhatta and Dang (2024b) [28] have also employed a QML algorithm to assess post-earthquake building integrity, classifying structures as safe or unsafe. The model was trained using simulation data derived from nonlinear time history analysis; a strategy employed to compensate the scarcity of real-world damage data. While this approach addresses data limitations, it may introduce potential biases that heavily depend on the quality of the simulated data. The model used a combination of seismic inputs, such as Peak Spectral Acceleration (PSA), and architectural features, including the number of stories and the years of construction, all normalized using a min-max scaler. Despite its innovation, the QML algorithm's performance was mixed, outperforming six classical supervised ML models but underperforming against four others, highlighting that while promising, QML's superiority is not yet fully observed in this context. A summary of the SHM studies mentioned in this section is shown in Table 1.

Table 1 - Overview of recent AI-powered studies for SHM. Signals (S), Image (I)

Ref.	Data type	Real scale structure	Quantum ML	Unsupervised	Detection	Localization	Quantification
Bisheh and Amiri (2023) [11]	S	✓			✓		
Chen *et al.* (2021) [12]	S				✓	✓	✓
Sony *et al.* (2022) [15]	S				✓	✓	
Civera *et al.* (2022) [16]	S			✓	✓		✓
Martucci *et al.* (2023) [17]	S	✓			✓		
Zhang *et al.* (2021) [18]	I	✓			✓	✓	

Zhao *et al.* (2022) [19]	I	✓			✓	✓	
Trochun *et al.* (2021) [25]	I	✓	✓		✓		
Correa-Jullian *et al.* (2022) [26]	S	✓	✓		✓		
Bhatta and Dang (2024a) [27]	I	✓	✓		✓	✓	✓
Bhatta and Dang (2024b) [28]	S	✓	✓		✓		
Ours	S	✓	✓	✓	✓	✓	✓

Regardless of its great possibilities, the QML real-world application in data-driven vibration SHM remains restricted. Besides, there are several works and methodologies developed in this context with crucial drawbacks, including neglecting the influence of environmental and operational conditions in the simulations, relying on simplistic numerical models for validation and utilizing supervised frameworks that may be impractical due to challenges in obtaining actual abnormal (i.e., damaged) training samples. As a result, there is a need for more robust and adaptable approaches that can account for the complexities and uncertainties inherent in real-world structural monitoring applications. To the best of the author's knowledge, to date, no other work has evaluated an unsupervised QML methodology applied to vibration-based SHM problems.

Hence, this work's unique contribution lies in a combination of (i) a new strategy for incorporating quantum circuits in unsupervised clustering-like manner in the field of vibration-based SHM, (ii) validation with experimental and real scale structures while also (iii) investigating anomaly detection, localization and quantification aspects. Additionally, this

study provides valuable insights about the comparative performance of the quantum-enhanced methodology versus a classical clustering technique, bringing light on the potential benefits and limitations of each approach. We also seek to advance on the field of SHM research by using experimentation and numerical analyses, laying the basis for future exploration and innovation at the edge of Quantum Computing and Civil Engineering. To this end, we explore both laboratory and full-scale experiments.

This paper is organized as follows: Section 2 introduces the fundamental concepts of Quantum Computing, providing readers with the necessary background knowledge about quantum bits, gates, and embedding techniques. In the sequence, Section 3 describes the methodology adopted, covering feature extraction techniques and the formulation of the proposed model. Section 4 presents the two experimental applications: a two-story laboratory frame and a real-scale railway bridge, followed by thorough analyses and discussion of results. Finally, Section 5 outlines the limitations and considerations of our study, and Section 6 presents the concluding remarks and discusses recommendations for future work.

2) Foundations of Quantum Computing

This section explores the essential prerequisites for understanding Quantum Computing and its intersection with Quantum Machine Learning. We provide an overview of Quantum Computing in Subsection 2.1, elucidating the fundamental concepts of vectors, quantum states and qubits. In Subsection 2.2, the discussion centers on operators, quantum gates, and entanglement, while Subsection 2.3 focuses on embedding techniques.

2.1) Quantum bits (Qubits)

The core of conventional systems in the computing field relies on bits, which are binary units representing either 0 or 1 at any given time. This is a deterministic approach where the state value is given by mutually exclusive conditions, such as whether a current flows across the circuit or if the voltage measurement is above or below a certain value. Such bits are employed to perform operations on logical gates (e.g., AND, OR, NOT, NAND, NOR, XOR and XNOR gates), which are the fundamental components of modern digital circuits, allowing the formulation of algorithms and setting the performance of a range of tasks.

On the other hand, Quantum Computing introduces a novel entity known as a quantum bit (or qubit), fundamentally reshaping our understanding of information processing. Unlike classical bits, qubits can exist in a superposition, meaning they can simultaneously embody both 0 and 1 states. This unique property not only expands the information capacity processing exponentially, but also enables quantum computers to perform parallel calculations and explore multiple possibilities at once.

The introduction of qubits into the computational landscape marks a departure from classical constraints and offers a look into a new era of computing. Some algorithms have the potential to solve complex problems at unprecedented speeds, such as reducing the spatial and temporal complexities that define the respective codes [29, 30]. In this sense, a qubit is represented mathematically as a vector inside a 2D complex space through an orthonormal basis. According to the terminology adopted by Quantum Mechanics, physical states are represented with the notation introduced by Dirac, where a vector is indicated with a "ket" $|\cdot\rangle$, while its dual counterpart is denoted by a bra $\langle . |$ [31].

The standard representation for vectors associated to "kets" and "bras" is usually expressed by the following matrices (also known as the computational basis):

$$|0\rangle = \begin{bmatrix}1\\0\end{bmatrix};\ |1\rangle = \begin{bmatrix}0\\1\end{bmatrix};\Rightarrow \langle 0| = [1\ 0];\ \langle 1| = [0\ 1]; \tag{1}$$

since dual vectors correspond to the conjugate transpose of the original matrix. To avoid any confusion, operators that act on a N dimension vector will be described as NxN matrices highlighted in bold color.

Note that the states defined in Eq. (1) obeys the orthonormalization rules for inner products, as $\langle 0|0\rangle = \langle 1|1\rangle = 1$ and $\langle 0|1\rangle = \langle 1|0\rangle = 0$. Hence, a single qubit's state can be defined as a linear combination of the computational basis in a single column [31] as

$$|\psi(t)\rangle = \alpha|0\rangle + \beta|1\rangle = \begin{bmatrix}\alpha\\\beta\end{bmatrix};\ \ \alpha,\beta \in \mathbb{C}, \tag{2}$$

where the wave function $|\psi\rangle$ satisfies the time-dependent Schrödinger´s equation for a given Hamiltonian operator **H**:

$$\mathbf{H}|\psi(t)\rangle = i\hbar\frac{\partial|\psi(t)\rangle}{\partial t} \Rightarrow |\psi(t)\rangle = \sum_{n=0}^{\infty}\frac{1}{n!}\left(\frac{-i\,(t-t_0)}{\hbar}\right)^{\boldsymbol{n}}\mathbf{H}^{\boldsymbol{n}}|\psi(t_0)\rangle \equiv e^{\frac{-i\mathbf{H}(t-t_0)}{\hbar}}|\psi(t_0)\rangle. \quad (3)$$

where $\hbar$ is the reduced Planck's constant.

On the other hand, the dual vector $\langle\psi(t)|$ is defined by a row as

$$\langle\psi(t)| = \alpha^*\langle 0| + \beta^*\langle 1| = [\alpha^*\ \beta^*]; \quad (4)$$

where $\alpha^*$and β^* are the respectively conjugate of the coefficients defined in Eq. (2). The notation $|\psi\rangle$ and $\langle\psi|$ will be maintained for simplification purposes, since the dependency of the parameter t in Eq. (3) is implicit on its coefficients [31].

Appendix A presents the algebraic procedure and statements required to define quantum states, observables, dynamics, probabilities and measurements through the Postulates of Quantum Mechanics. According to these postulates, the normalizing condition for a wave vector is required since a quantum system may only collapse to one of the basis states, with a probability (before the measurement process) that is proportional to the square of its respectively amplitude. Hence, the complex numbers α and β satisfy the relation

$$\langle\psi|\psi\rangle = |\alpha|^2 + |\beta|^2 = 1, \quad (5)$$

where $|\alpha|^2$ and $|\beta|^2$ are the respective probabilities to find the qubits in the states $|0\rangle$ and $|1\rangle$ after a measurement projected on the computational basis.

The Bloch sphere shown in Fig. 1 is the most useful tool to visualize any configuration that may be assumed by a single quantum state. From this point of view, the formal representation of a qubit is described by spherical coordinates parameters θ and φ as

$$|\psi\rangle = \cos\frac{\theta}{2}|0\rangle + \sin\frac{\theta}{2}e^{i\varphi}|1\rangle, \quad (6)$$

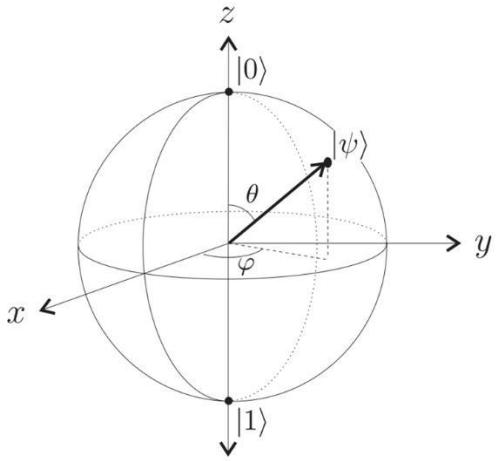

Figure 1 - Bloch sphere representation of a qubit associated to a particular wave function $|\psi\rangle$. Adapted from Kaye et. al. (2007) [31].

For systems composed of multiple qubits, the global wave function is formally described by a sequence of tensor product as

$$|\Psi\rangle = |\psi_1\rangle \otimes |\psi_2\rangle \otimes \cdots \otimes |\psi_N\rangle. \quad (7)$$

In this case, $|\Psi\rangle$ is represented by a column vector with 2^N rows, where the *i*-th state in the ordered sequence from $|0_1\rangle \otimes |0_2\rangle \otimes \cdots \otimes |0_N\rangle$ to $|1_1\rangle \otimes |1_2\rangle \otimes \cdots \otimes |1_N\rangle$ is associated to the respective amplitude probability located at the *i*-th row. For the sake of simplicity, the tensor $\otimes$ will be omitted from now on, and the aforementioned states will be presented according to the compressed standard notation as $|00\cdots0\rangle$ to $|11\cdots1\rangle$ (considering that the vector dimension is implicit on each definition).

With the appropriate operations performed by specific quantum gates, it is possible to represent a superposition of all those states simultaneously. This capability opens doors to various applications of Quantum Computing with significant consequences for computational efficiency and problem-solving across diverse fields, as discussed in the next subsection.

2.2) Quantum gates

Quantum gates are the components that enable handling qubits by exploring properties that are not allowed by its classical counterparts. They are expressed as unitary matrices **U** and provide the basic techniques by which states can be altered to execute computing assignments. In fact, the effect of **U** on $|\Psi\rangle$ (Eq. (7)) can be visualized in the Bloch sphere as rotating the

initial wave vector to align it with the one described by $\mathbf{U}|\Psi\rangle$ [32]. Throughout this subsection, we discuss the main single and multiple-qubit operations.

For any operator $\mathbf{O}$ and arbitrary quantum states $|\psi\rangle$ and $|\varphi\rangle$, there is a corresponding operator $\mathbf{O}^{\dagger}$ such that

$$\langle\psi|\mathbf{O}\varphi\rangle = \langle\varphi\mathbf{O}^{\dagger}|\psi\rangle, \tag{8}$$

where $\mathbf{O}^{\dagger}$ is called the adjoint or conjugate Hermitian of $\mathbf{O}$. In this sense, $\mathbf{O}^{\dagger}$ is represented as a square matrix in the dual space, where each element at the *i*-th row and *j*-th column is equal to the conjugate transpose of the original matrix $\mathbf{O}$, i.e., $\mathbf{O}^{\dagger}_{\boldsymbol{ij}} = \mathbf{O}^{*}_{\boldsymbol{ji}}$.

An operator is said to be Hermitian if $\mathbf{O} = \mathbf{O}^{\dagger}$. In this case, the respectively eigenvalues λ_i are always real numbers, which becomes evident when $\mathbf{O}$ is expressed in its diagonal form (as $\lambda_i = \lambda_i^*$). These variables are called "observables", since the eigenvalues are associated to physical parameters that can be measured along the information processing [32].

In turn, a unitary operator $\mathbf{U}$ has normalized complex eigenvectors ($|\lambda_i| = 1$) and obeys the condition

$$\mathbf{U}\mathbf{U}^{\dagger} = \mathbf{U}^{\dagger}\mathbf{U} = \boldsymbol{I}, \tag{9}$$

where the conjugate Hermitian plays the role of the inverse operator of $\mathbf{U}$: $\mathbf{U}^{\dagger} = \mathbf{U}^{-\mathbf{1}}$. Hence, according to Eqs. (3) and (9), the wave function evolution can be described by unitary transformations $\mathbf{U} \equiv e^{\frac{-i\mathbf{H}(t-t_0)}{\hbar}}$ and $\mathbf{U}^{\dagger} \equiv e^{\frac{i\mathbf{H}(t-t_0)}{\hbar}}$ that preserves the norm predicted by Eq. (5): $\langle\psi(t)\mathbf{U}^{\dagger}|\mathbf{U}\psi(t)\rangle = \langle\psi(t_0)\mathbf{U}^{\dagger}|\mathbf{U}\psi(t_0)\rangle = 1$. For this reason, quantum gates are usually associated with unitary Hermitian matrices ($\mathbf{U} = \mathbf{U}^{\dagger}$), which ensure that measurement outputs will be real and satisfy the reversibility criteria ($\mathbf{U} = \mathbf{U}^{-\mathbf{1}}$) for logical operations.

Let us start describing the most common operations that act on a single qubit. The first set of gates is given by the Pauli matrices:

$$\boldsymbol{\sigma}_{\mathbf{x}} = \begin{bmatrix} 0 & 1 \\ 1 & 0 \end{bmatrix} = |0\rangle\langle 1| + |1\rangle\langle 0| \Rightarrow \boldsymbol{\sigma}_{\mathbf{x}}|0\rangle = |1\rangle;\ \boldsymbol{\sigma}_{\mathbf{x}}|1\rangle = |0\rangle; \tag{10}$$

$$\boldsymbol{\sigma}_{\mathbf{y}} = \begin{bmatrix} 0 & -\mathrm{i} \\ \mathrm{i} & 0 \end{bmatrix} = -i|0\rangle\langle 1| + \mathrm{i}|1\rangle\langle 0| \Rightarrow \boldsymbol{\sigma}_{\mathbf{y}}|0\rangle = \mathrm{i}|1\rangle;\ \boldsymbol{\sigma}_{\mathbf{y}}|1\rangle = -i|0\rangle;$$

$$\boldsymbol{\sigma_z} = \begin{bmatrix} 1 & 0 \\ 0 & -1 \end{bmatrix} = |0\rangle\langle 0| - |1\rangle\langle 1| \Rightarrow \boldsymbol{\sigma_z}|0\rangle = |0\rangle;\ \boldsymbol{\sigma_z}|1\rangle = -|1\rangle.$$

In fact, $|0\rangle$ and $|1\rangle$ are defined as the eigenstates of the $\boldsymbol{\sigma_z}$ operator, whose eigenvalues $+1$ and -1 are the respectively outputs associated to the projectors $\mathbf{P_0} = |0\rangle\langle 0|$ and $\mathbf{P_1} = |1\rangle\langle 1|$. Together with the Identity matrix, the Pauli operators constitute an orthonormal set to represent any $2x2$ matrix [33].

On the one hand, note that the action of σ_x in Eq. (10) is similar to the classical gate NOT, as it flips the states $|0\rangle$ and $|1\rangle$. On the other hand, σ_y and σ_z have no classical analogues, since the respective local phases $\pm i$ and -1 embedded in the outputs are purely quantum. Also note that the Pauli operators are reversible and obey a recursive relation, since $\boldsymbol{\sigma_k}^2 = \mathbf{I}$ for $k = \{x, y, z\}$ and $\boldsymbol{\sigma_1\sigma_2} = \varepsilon\boldsymbol{\sigma_3}$, where ε is the Levi-Civita symbol referring to the indices ordered in k.

Another operation that is widely used in many quantum algorithms is represented by the Hadamard gate $\boldsymbol{H}$, which rotates the states $|0\rangle$ and $|1\rangle$ into a superposition of the computational basis with equal probability amplitudes. This property enables the qubit to assume a configuration whose components contribute simultaneously to both states until it is measured [33], and its matrix representation is given by

$$\boldsymbol{H} = \frac{1}{\sqrt{2}}\begin{bmatrix} 1 & 1 \\ 1 & -1 \end{bmatrix} \Rightarrow \boldsymbol{H}|0\rangle = \frac{|0\rangle + |1\rangle}{\sqrt{2}} = |+\rangle;\ \boldsymbol{H}|1\rangle = \frac{|0\rangle - |1\rangle}{\sqrt{2}} = |-\rangle. \qquad (11)$$

Note that the states $\{|+\rangle; |-\rangle\}$ also form an orthonormal basis and, as well as for Pauli matrices, two consecutive applications of the Hadamard gate cancel each other out ($\boldsymbol{H}^2 = \mathbf{I}$) and restore the original state of the qubit.

In general, all operations that act on single qubits can be generated through gates that correspond to rotations about the x-, y-, and z-axes of the Bloch sphere (Fig. 1) by a specific angle. These sets are defined for arbitrary parameters $\{\alpha, \beta, \gamma\} \rightarrow [0; 2\pi]$ [34] as

$$\mathbf{R_x}(\alpha) = \begin{bmatrix} \cos\frac{\alpha}{2} & -i\sin\frac{\alpha}{2} \\ -i\sin\frac{\alpha}{2} & \cos\frac{\alpha}{2} \end{bmatrix};\ \mathbf{R_y}(\beta) = \begin{bmatrix} \cos\frac{\beta}{2} & -\sin\frac{\beta}{2} \\ \sin\frac{\beta}{2} & \cos\frac{\beta}{2} \end{bmatrix};\ \mathbf{R_z}(\gamma) = \begin{bmatrix} e^{-i\frac{\gamma}{2}} & 0 \\ 0 & e^{i\frac{\gamma}{2}} \end{bmatrix}; \tag{12}$$

which can be summarized by the general rotations expressed in a single matrix as

$$\mathbf{U_3}(\theta, \varphi, \lambda) = \begin{bmatrix} \cos\frac{\theta}{2} & -e^{i\lambda}\sin\frac{\theta}{2} \\ e^{i\varphi}\sin\frac{\theta}{2} & e^{i(\varphi+\lambda)}\cos\frac{\theta}{2} \end{bmatrix}; \tag{13}$$

where $\{\theta, \varphi, \lambda\}$ are bound to the interval [0; π] [35].

In turn, two-qubit gates leverage the concept of superposition and entanglement to perform operations over bipartite systems. In this context, the specific class of controlled gates – where the state of one qubit (set as the control) influences another (chosen as the target) – plays a key role towards these goals. The most representative example is the Controlled-Not (**CNOT**) gate, which reproduces the action of the $\boldsymbol{\sigma_x}$ operator under the standard following conditions:

- When the control qubit is in the state $|0\rangle$, the target qubit state remains unchanged.
- When the control qubit is in the state $|1\rangle$, the target qubit state is toggled.

These rules can be described by the following matrix and the subsequent relations:

$$\mathbf{CNOT} = \begin{bmatrix} 1 & 0 & 0 & 0 \\ 0 & 1 & 0 & 0 \\ 0 & 0 & 0 & 1 \\ 0 & 0 & 1 & 0 \end{bmatrix} = |00\rangle\langle 00| + |01\rangle\langle 01| + |10\rangle\langle 11| + |11\rangle\langle 10| \Rightarrow \tag{14}$$

CNOT $|00\rangle$=$|00\rangle$; **CNOT** $|01\rangle$=$|01\rangle$; **CNOT** $|10\rangle$=$|11\rangle$; **CNOT** $|11\rangle$=$|10\rangle$;

where the set $\{|00\rangle; |01\rangle; |10\rangle; |11\rangle\}$ represents the computational basis for bipartite systems.

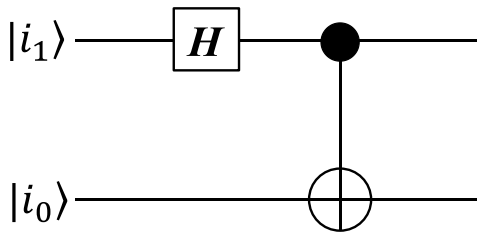

Figure 2 - Circuit designed to generate a bipartite entangled state. Adapted from Benenti et al. (2007) [34].

Fig. 2 shows the simplest circuit designed to generate a bipartite entangled state, where the input $|i_0\rangle|i_1\rangle$ (from bottom to top) is assumed to describe any arbitrary configuration. In turn, the standard **CNOT** is defined by a black dot (control) connected to an empty circle (target), which indicates that the gate is activated only if the control qubit is $|1\rangle$. Hence, when $|i_1\rangle$ passes through the Hadamard gate, its state is changed to a superposition of the computational basis $|0\rangle$ and $|1\rangle$. Consequently, the component associated to $|0\rangle|i_0\rangle$ is not altered, whereas the state of the target in $|1\rangle|i_0\rangle$ is flipped.

This phenomenon described above is called **entanglement** [34], where the state of each qubit becomes intrinsically linked to the other. When the input $|i_1\rangle|i_0\rangle$ is defined as the computational basis for bipartite systems (Eq. (13)), the circuit´s output is given by four possibilities regarding maximally entangled bipartite states

$$|\Phi^+\rangle = \frac{|00\rangle + |11\rangle}{\sqrt{2}};\ |\Phi^-\rangle = \frac{|00\rangle - |11\rangle}{\sqrt{2}};$$
$$|\Psi^+\rangle = \frac{|01\rangle + |10\rangle}{\sqrt{2}};\ |\Psi^-\rangle = \frac{|01\rangle - |10\rangle}{\sqrt{2}}; \tag{15}$$

which forms the Bell basis and plays a crucial role for most quantum algorithms [32]. Note that $|\Phi^+\rangle$ and $|\Phi^-\rangle$ are defined as a superposition of qubits in a symmetric configuration that are equally likely to be measured ($|00\rangle$ and $|11\rangle$), while $|\Psi^+\rangle$ and $|\Psi^-\rangle$ describes a pair of orthogonal states ($|01\rangle$ and $|10\rangle$) with the same probability.

Since all multi-qubit operations can be performed with **CNOT** and single qubit gates [32], the concepts and theoretical tools presented here are addressed in the analysis of the algorithms covered in this work. In the following subsection, we discuss specific techniques to process classical data in quantum algorithms.

2.3) Quantum embedding techniques

One of the biggest challenges emerges when one must feed classical data in a quantum algorithm due to the need to adapt the input properly to the quantum hardware. For this purpose, embedding techniques are used to represent classical features into quantum states to serve as the circuit input, so that quantum computers can manipulate information through physical qubits. While a variety of quantum encoding methods exist, each has its unique advantages and constraints [36], and the field continues to be an active area of research. In this subsection, two typical encoding techniques are briefly discussed: angular and amplitude encodings.

On the one hand, angle encoding exploits the inherent phase and the properties of qubits to process the information. This method employs rotation gates **R** to convert a classical data x (representing a given data point) [36] to a quantum state with n qubits as

$$x \to |x\rangle = \mathbf{R}(x_1) \otimes \mathbf{R}(x_2) \cdots \mathbf{R}(x_i) \cdots \mathbf{R}(x_{n-1}) \otimes \mathbf{R}(x_n), \tag{16}$$

where the symbol $\otimes$ denotes the tensor product between the n individual rotations applied to each qubit. These gates can perform the operations detailed in Eq. (12): $\mathbf{R_x}$, $\mathbf{R_y}$ or $\mathbf{R_z}$, which are attached separately to each qubit by adjusting the rotation angle to produce the desired state $|x\rangle$. For a better understanding, a step-by-step numerical example of encoding classical data into quantum states is provided in Appendix B. While this scheme may not be as robust in terms of encoding capacity compared to others, it stands out for its simplicity in configuration, which makes it widely adopted. This technique is frequently employed in QML models for data classification [37], as well as in QNNs [38].

On the other hand, amplitude encoding creates and maps different phases for bits, as it converts a classical input vector x (of length N) into the amplitudes of an n-qubit state with $n = log_2(N)$. This operation is defined by [37]

$$x \to |x\rangle = \frac{1}{\|\mathbf{x}\|} \sum_{i=1}^{2^n} x_i |i\rangle, \tag{17}$$

where the states $|i\rangle$ are associated with a given basis. The main representative example is the action of the Hadamard gate (Eq. (11)) over the n qubits when $|x\rangle$ is expressed in the computational basis, which generates a superposition of all possible states between $|0_1\rangle \otimes$

$|0_2\rangle \otimes \cdots \otimes |0_N\rangle$ and $|1_1\rangle \otimes |1_2\rangle \otimes \cdots \otimes |1_N\rangle$ with an amplitude probability proportional to $1/\sqrt{2^n}$.

3) Methodology

The current SHM methodology involves collecting vibration data two structures of interest. The acceleration measurements are processed to extract relevant information from the signal responses, and the ones collected under reference conditions (e.g., undamaged) are compared to those captured under unknown scenarios (e.g., damaged) using an unsupervised quantum classifier. In Subsection 3.1, we outline the process to extract statistical features from data to encode them into quantum states. Next, we apply Quantum Machine Learning (QML) techniques in Subsection 3.2 to analyze the chosen dataset. Finally, we present a comprehensive framework of the proposed methodology in Subsection 3.3.

3.1) Feature extraction

Feature extraction serves as a critical stage in structural damage identification problems, where the focus lies in extracting relevant information from the signals acquired from sensors or monitoring systems. An effective feature extraction procedure guarantees that the data are transformed into a format that highlights their key characteristics, which can be used to distinguish normal from abnormal structural behaviors [39]. Based on this premise, the present study employs time domain features obtained from raw acceleration data regarding 11 statistical features $\boldsymbol{x_{t,i}}$ extracted from vibration signals $\boldsymbol{y_i}$, as shown in Table 2.

The selection of these specific waveform features was motivated by their capacity to capture both linear and nonlinear aspects of vibration signals. They were proposed by the well stablished book of Farrar and Worden [40], which emphasizes that statistical features derived from time-domain data are particularly advantageous in SHM, as they can detect subtle changes in structural behavior that may precede visible damage. Additionally, these features offer simplicity, computational efficiency, and direct interpretability. A deeper look at the relevance of selected feature set reveals that lower-order statistics, such as mean and variance, represents the central tendency and dispersion of the data. Conversely, higher-order statistics (HOS), such as skewness and kurtosis, represent the asymmetry of the data distribution, which are sensitive

to transient events. Previous research has shown that HOS performs considerably well in SHM applications, as presented in the works developed by [39-44].

Table 2 - Statistical features x_i extracted from signal y_i

Statistic	Definition
Peak [42-44]	$x_{1,i} = \max(\boldsymbol{y_i})$
Mean [43, 44]	$x_{2,i} = \frac{1}{N}\sum_{i=1}^{N} \boldsymbol{y_i}$
Mean Square [43, 44]	$x_{3,i} = \frac{1}{N}\sum_{i=1}^{N} \boldsymbol{y_i^2}$
Root mean square [41-44]	$x_{4,i} = \left(\frac{1}{N}\sum_{i=1}^{N} \boldsymbol{y_i^2}\right)^{\frac{1}{2}}$
Squared mean root [44]	$x_{5,i} = \left(\frac{1}{N}\sum_{i=1}^{N} \lvert\boldsymbol{y_i}\rvert^{\frac{1}{2}}\right)^{2}$
Variance [40, 43, 44]	$x_{6,i} = \frac{1}{N-1}\sum_{i=1}^{N} \lvert\boldsymbol{y_i} - x_{2,i}\rvert^{2}$
Standard deviation [43, 44]	$x_{7,i} = \sqrt{x_{6,i}}$
Skewness [41, 43, 44]	$x_{8,i} = \frac{\sum_{i=1}^{N}(\boldsymbol{y_i} - x_{2,i})^3}{(N-1)(x_{7,i})^3}$
Kurtosis [41-44]	$x_{9,i} = \frac{\sum_{i=1}^{N}(\boldsymbol{y_i} - x_{2,i})^4}{(N-1)(x_{7,i})^4}$
Crest Factor [41-44]	$x_{10,i} = \frac{\max(\lvert\boldsymbol{y_i}\rvert)}{x_{4,i}}$
Shape factor [41, 42, 44]	$x_{11,i} = \frac{x_{4,i}}{\frac{1}{N}\sum_{i=1}^{N}\lvert\boldsymbol{y_i}\rvert}$

3.2) Unsupervised QML

The method used in the present paper is named Quantum Variational Rewinding algorithm (or QVR), which is adapted from the work of Baker et al. (2022) [45]. Based on

previously established limits, its purpose consists in distinguishing a given data distribution between a pattern considered normal and an anomalous one. Initially, the method was conceived to deal only with time series. For this reason, we choose to use statistical features as inputs to the quantum states, where the main benefit of such a strategy is to reduce the processing power and memory necessary to run the algorithms.

Before applying the QVR algorithm, we first establish a set of values x^{normal} defined as a reference for a normal distribution, which represents the temporal behavior of a system under regular conditions. Then, we train a chosen network with the same data to generate a function $a_{x^{normal}}(x)$ that indicates the anomaly score for all $x \in x^{normal}$, where the condition $a_{x^{normal}}(x) \approx 0$ must be satisfied for every input. Next, we feed the system with a new dataset x^{unkown} to test the effectiveness of the model with a previously defined threshold $\zeta \in \mathrm{R}$. If $a_{x^{normal}}(x^{unkown}) > \zeta$ for any subset of the input data, the set is classified as anomalous; otherwise, the series meets the expected requirements of a normal distribution.

Now, let us illustrate the method by considering a set of T-many features classical data $\boldsymbol{x} = (\boldsymbol{x_t}: t \in T)$ from a given time series $\boldsymbol{y} = (\boldsymbol{y_i}: i \in Z^{+}_{\leq p})$ obtained after p-many observations, where p is a positive integer. The first stage consists in converting the whole set into a sequence $S = (|x_t\rangle: t \in \mathrm{T})$ of n-qubit quantum states representing $\boldsymbol{x}$. To this end, we build a quantum circuit starting with all inputs equal to $|0\rangle$, and then evolve each one with a quantum feature map through a unitary operator $\mathbf{U}(x_t)$. This stage can be associated to an unknown embedding Hamiltonian $\mathbf{H_E}$, where each component generated in this process corresponds to an element of S [45]:

$$|x_t\rangle = \mathbf{U}(x_t)|0\rangle^{\otimes n} \equiv e^{-i\mathbf{H_E}(x_t)}|0\rangle^{\otimes n}. \tag{18}$$

In the following step, all states $|x_t\rangle$ are subjected to a new dynamic described by another unitary operator $\mathbf{V_t}(\alpha, \gamma)$, which is also associated with an unknown Hamiltonian $\mathbf{H}(\alpha, \gamma)t$:

$$|x_t, \alpha, \gamma\rangle = \mathbf{V_t}(\alpha, \gamma)|x_t\rangle \equiv e^{-i\mathbf{H}(\alpha,\gamma)t}|x_t\rangle. \tag{19}$$

In this case, $\mathbf{V_t}(\alpha, \gamma) \equiv e^{-i\boldsymbol{H}(\alpha,\gamma)t}$ can be written as an eigendecomposition of the respective matrices of eigenvectors $\mathbf{W}(\alpha)$ and its diagonalized form $\mathbf{D}(\gamma, t)$:

$$\mathbf{V_t}(\alpha,\gamma) = \mathbf{W}^{\dagger}(\alpha)\mathbf{D}(\gamma,t)\mathbf{W}(\alpha), \tag{20}$$

where γ represents the eigenvalues of $\mathbf{H}(\alpha,\gamma)t$ [45].

For the method to succeed, the original statement $a_{x^{normal}}(x) \approx 0$ must be satisfied for every non-anomalous behavior. This condition can be fulfilled by imposing the restriction $|x_t,\alpha,\gamma\rangle \approx |0\rangle^{\otimes n}$ for normal distributions, which is equivalent to ensure that the probability associated to measuring the qubits at the end of the process satisfies $|\langle 0|^{\otimes n}|x_t,\alpha,\gamma\rangle|^2 \approx 1$. Consequently, from Eqs. (18-20):

$$\begin{aligned}\langle 0|^{\otimes n} e^{-i\mathbf{H}(\alpha,\gamma)t} e^{-i\mathbf{H_E}(x_t)}|0\rangle \approx 1 \Rightarrow e^{-i\mathbf{H}(\alpha,\gamma)t} e^{-i\mathbf{H_E}(x_t)} \approx \mathbf{I} \Leftrightarrow\ & \mathbf{H}(\alpha,\gamma)t \\ \approx\ & -\mathbf{H_E}(x_t),\end{aligned} \tag{21}$$

i.e., the Hamiltonians must be anti-symmetric and the parameterized unitary operator $\mathbf{V_t}(\alpha,\gamma)$ should be able to *rewind* each state $|x_t\rangle$ to the global initial input defined as $|0\rangle^{\otimes n}$.

In practice, it is impossible for a single Hamiltonian to successfully rewind every $x \in x^{normal}$, as they are univocally defined. On the other hand, we can calculate the expected value generated by many Hamiltonians [46] through the function

$$F(\phi,x_t) = E_{\gamma\sim N(\mu,\sigma)}\left[\langle 0|^{\otimes n}|x_t,\alpha,\gamma\rangle\right], \qquad \phi = [\alpha,\mu,\sigma], \tag{22}$$

considering that $F(\phi,x_t) \approx 1$ for all $x \in x^{normal}$ and $t \in T$. For each case, the parameter γ is selected from a normal distribution $N(\mu,\sigma)$ with mean μ and standard deviation σ.

Next, we can define the loss function $\mathcal{L}(\phi)$ to minimize the mean square error in Eq. (22) as:

$$\mathcal{L}(\phi) = \frac{1}{2|x^{normal}||T|}\sum_{x\,\in\,x^{normal}}\sum_{t\,\in\,T}[1-F(\phi,x_t)]^2 + P_\tau(\sigma), \tag{23}$$

where the factor $1/2|x^{normal}||T|$ ensures the normalization condition for $\mathcal{L}(\phi)$, whereas the function $P_\tau(\sigma)$ (set with a single hyperparameter τ) penalizes large values of σ [46].

Finally, the anomaly score function $a_{x^{normal}}(x^{unkown})$ is defined as:

$$a_{x^{normal}}(x^{unkown}) = \frac{1}{|T|}\sum_{t \in T}[1 - F(\phi^*, x_t^{unknown})]^2, \quad (24)$$

where $\phi^*$is the argument established through a classical optimization routine that minimizes $\mathcal{L}(\phi)$ in Eq. (23).

In this sense, we can train a clustering algorithm with the results provided by Eq. (24) with normal features $x \in x^{normal}$ to produce a cluster $F(\phi^*, x_t)$ centered at 1. Therefore, if $F(\phi^*, x_t) \gg 1$ for a new dataset $x^{unknown}$, the pattern will be classified as an anomalous distribution. For a more detailed understanding about the algorithm iterations, training loops and classification, “Appendix C: Unsupervised QML Pseudocodes” is advised. Furthermore, "Appendix D: List of customizable parts of QML" aims to serve as a baseline for future researchers to investigate and replicate the experiments with other hyperparameters.

3.2.1 Tuning the threshold

During the process of tuning the threshold ζ explained in Subsection 3.2, the parameter is adjusted to optimize a chosen metric through the comparison between a normal and an unknown time series. In this study, an accuracy score is defined as the reference to be optimized, where the anomaly score function $a_{x^{normal}}(x^{unkown})$ obtained from the previous unsupervised training phase is applied to a new data to search values for ζ along a refined sampled one-dimensional grid. Since our goal is to identify the results that yield the highest accuracy score, anomalies are classified according to higher increasing limits, while normal behaviors (i.e., undamaged) are assigned to patterns whose maximum values do not surpass a rate of 50%, which represents the baseline randomness of a binary classification.

3.3) Proposed framework

A visual representation of the main steps and components involved in the proposed approach is illustrated in Fig. 3. The procedure starts by collecting acceleration measurements from a network of sensors placed all over the structure under investigation (Fig. 3(a)). The vibration responses are then split into signal samples, which is followed by a feature extraction process conducted on the raw dynamic data. The method generates 11 statistical indicators for the respectively signal samples collected from each sensor (Fig. 3(b)), which are essential to capture the fundamental properties of the dynamic behavior of the structure. Note that the whole procedure must be performed for both intact (which is previously known) and unknown signals.

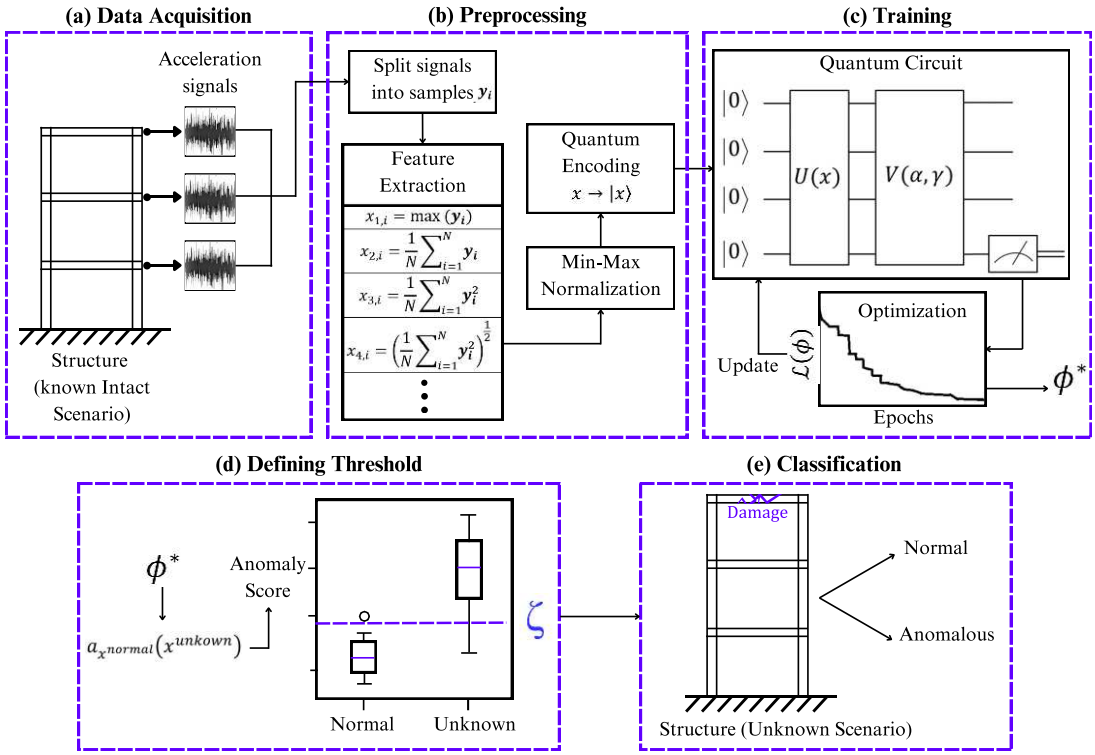

Figure 3 – Overview of the methodology steps.

However, features with different units of measurement across the signals can be problematic, as it introduces a bias that may affect the model's performance. An alternative is to employ dimensionless variables, which should have similar interval sizes to prevent one or more features from dominating the classification model. In this sense, many effective strategies can be adopted, such as ratios between features, dividing by a reference value, or employing *min-max* scaling or normal standardizations (also known as the *z*-score normalization).

For this study, the *z*-score normalization may not be particularly useful, as there is no guarantee that the features extracted from various structures follow a normal distribution. Conversely, a *min-max* normalization process can be considered suitable [28], wherein each feature is scaled within the interval [0,1] based on its original range. This choice solves the initial restriction, as it ensures that all variables must have equal weight (since they exhibit the same range lengths). Hence, for a given feature x_i, the *min-max* normalization is defined as

$$x_i^{scaled} = \frac{x_i - \min(\boldsymbol{x})}{\max(\boldsymbol{x}) - \min(\boldsymbol{x})}. \tag{25}$$

The next step consists in encoding the scaled features that will serve as inputs for the quantum circuit (Fig. 3(b)). As discussed in Subsection 2.3, this operation is required because it allows the features extracted from the sensor data to be represented in a quantum formalism, enabling it to be processed and analyzed by the proposed quantum algorithm. The corresponding quantum circuit is illustrated in Fig. 4. While the first block (indicated by $U(x)$) represents the unitary operation responsible to encode the features, the second ($V(\alpha,\gamma)$) contains the unitary operator build to train the parameters that will be optimized. When $U(x)$ and $V(\alpha,\gamma)$ are expressed as controlled gates that act simultaneously on two or more qubits (Fig. 2), the respectively quantum states get entangled (see Eq. (15)).

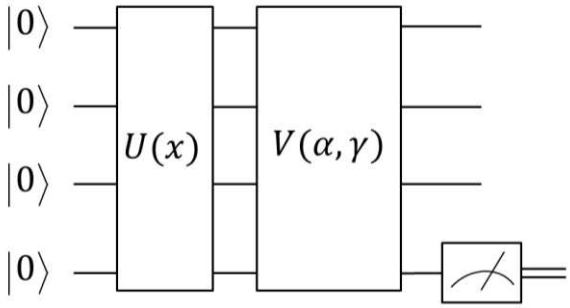

Figure 4 – General structure of the quantum circuit architecture.

By considering only the known intact scenario features as the training set, we define a loss function (Eq. (23)) to measure the discrepancy between the actual and expected quantum states, which is bound to penalize large deviations. Afterwards, the training process (illustrated in Fig. 3(c)) is performed to minimize $\mathcal{L}(\phi)$ with classical optimization techniques. Then, an anomaly score function is evaluated (Eq. (24)), which is fitted specifically to quantify deviations from the normal behavior (defined with the features extracted previously) from the known intact signal. This function is designed to identify anomalies when the variables deviate significantly from the normal center, i.e., the anomaly score tends to vanish in normal situations and increases when it is far from the normal center. Note that these rules guarantee the unsupervised premise of our methodology.

In summary, the proposed approach converts the problem of anomaly detection into a clustering approach in the quantum space. By training the model on normal feature instances, we can identify deviations from the expected behavior and point out potential structural anomalies. Moreover, like many ML algorithms, the training process is conducted using mini-batches, whose default parameters are set as follows: Batch size: 10; Optimizer: *Adam*;

Learning rate: 0.01; Batch iterations: 1000 and $W(\alpha)$ layers: 2. Moreover, *Python* is the primary language used to implement the current QML computations, more specifically through the *Jupyter Notebook* environment and within the *Google Colaboratory* platform. In turn, codes are processed on the standard cloud CPU to ensure reproducibility with the following specifications: *Intel(R) Xeon(R)* 2.20GHz and 12.7 GB of RAM. Due to the instability of the near-term Quantum Computing devices [47] known as NISQ (from Noisy Intermediate-Scale Quantum), tests were carried out on quantum simulators to provide more reliable results, since the former have few qubits available in open access accounts as the ones provided by the IBM Experience Platform [35].

Regarding computational libraries, we focused on *Pennylane*, *PyTorch* and *Covalent*. The first is chosen to run codes in a quantum simulator, whereas *PyTorch* supports the optimization of trainable quantum parameters through *Adam Optimizer*. Conversely, *Covalent* manages the interaction between these systems by distributing different tasks to distinct computational resources and integrating them into a specific workflow. Given that QML algorithms involve both classical and quantum computing resources, *Covalent* is essential to provide the required heterogeneity along this process. Additionally, *MATLAB* independent routines are developed to complement these tasks, such as data preprocessing, visualization, preparation and comparison by the K-means and hierarchical clustering method.

In this study, half of the known healthy data are utilized solely for fine-tuning the anomaly score function $a_{x^{normal}}(x^{unkown})$ and the other half for testing. After establishing this dependency, the parameters of the quantum circuit responsible for processing data remain unchanged for subsequent testing. When the algorithm is executed on unknown scenarios, a threshold value (ζ) is established to enhance the detection of anomalies (as described in Subsection 3.2.1 and illustrated in Fig. 3(d)). In this sense, our goal consists in adjusting ζ seeking to achieve the highest accuracy allowed to distinguish between the known datasets from any unknown sequence. Besides, for all applications analyzed, data instances are randomized to avoid any undesired bias. Hence, for a given unknown scenario, half of the testing data is allocated for tuning the threshold ζ, while the remaining is used to assess the algorithm's classification accuracy (Fig. 3(e)). This approach aims to prevent overfitting and ensures that the algorithm generalizes properly to new unseen scenarios beyond the training data.

Finally, the classification of each signal unknown sample by the algorithm is described according to the true labels:

$$\text{Signal sample classification} = \begin{cases} \text{Anomalous}, & if \quad a_{x^{normal}}\left(x^{unkown}\right) > \zeta\,; \\ \text{Normal}, & Otherwise; \end{cases} \tag{26}$$

whereas the accuracy is determined by

$$\text{Accuracy} = \frac{TP}{TP + FP}\,; \tag{27}$$

where *TP* and *FP* respectively stand for true and false positives. For cases where the unknown data are healthy, it is expected that the algorithm will struggle to differentiate and will produce a nearly random binary classification, i.e., approximately 50% accuracy. Conversely, if the unknown data contain anomalies, the algorithm should separate data more effectively, resulting in a higher accuracy. Consequently, Eqs. (26) and (27) serve as an index for assessing damage, and this approach ensures that the algorithm remains unsupervised to autonomously detect and analyze structural anomalies. Moreover, the proposed methodology is evaluated on structures subject to two stages of progressive structural abnormalities. Therefore, this allows assessing not only the algorithm's ability to quantify damage but also to differentiate patterns of increasing structural degradation.

4) Applications

Two experiments are used to assess the proposed methodology's performance: a 2-story slender frame (Subsection 4.1) and the KW51 railway bridge (Subsection 4.2). By testing both laboratory and real-scale structures subject to progressive anomaly events and single damage scenarios, the study aims to simulate realistic conditions where structural integrity may be compromised. In both applications, an additional intact scenario, not included in the training phase, is introduced to assess the models' susceptibility to overfitting. This approach aims to improve the classifier's generalization capabilities, ensuring more reliable outcomes. Such investigations are expected to provide insights into the method's robustness and applicability in detecting and characterizing structural abnormalities, thereby advising on its potential for real-world structural health monitoring applications.

4.1) 2-story laboratory frame

The configuration of the two-story slender aluminum frame is depicted in Fig. 5. Its bar elements are linked using screws, washers, and nuts of equal specifications: 300 mm long, 15.875 mm wide, and 1.587 mm thick [48]. The schematic of the experimental setup is displayed in Fig. 5(a). It consists of four unidirectional Bruel© piezoelectric Integrated Electronics Piezoelectric (IEPE) accelerometers positioned at the marked locations on the structure to record horizontal accelerations. Each sensor has a sensitivity of 100 mV/g and a low-pass filter was configured with a cutoff frequency of 100 Hz. To apply the load, a pendulum with a mass of 14 g was attached to the top. The loading process consisted in releasing the pendulum from rest from a predefined position and letting it collide to the frame at 180mm from the ground (see Fig. 5(b)). The three structural conditions examined in the current study are described in Table 3. For more information, the reference Finotti *et al*. (2023) [48] is advised.

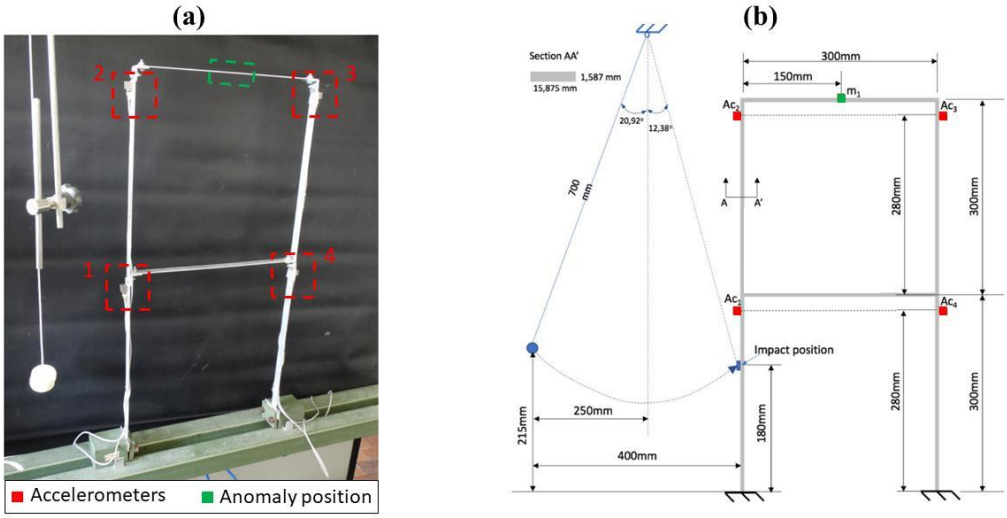

Figure 5 - (a) Photo of the two-story laboratory frame and (b) dimensions. Adapted from Finotti et al. (2023) [48].

Table 3 - Structural conditions of two-story laboratory frame

Situation	Description
Intact scenario	Baseline
Unknown intact scenario	No mass added
Damage scenario I	Mass added at the second floor (7.81 g)
Damage scenario II	More mass added at the second floor (15.62 g)

One hundred (100) tests were performed for each structural condition, yielding 400 in total. Furthermore, each accelerometer had 2000 sampled points, with the largest peak of acceleration acting as the starting point. This window aims to capture strong impact amplitudes while ignoring low energy signals that result from decreasing responses until stationary vibration. The data were recorded at a frequency of 500 Hz, such that each sample had a length of four seconds. A typical signal and its frequency response are shown in Fig. 6 and Fig. 7, respectively. The selection of the data acquisition rate at 500 Hz was decided after a preliminary assessment of the signal's bandwidth, structural dynamics, accuracy requirements, and data storage constraints, according to Finotti et al. (2023) [48].

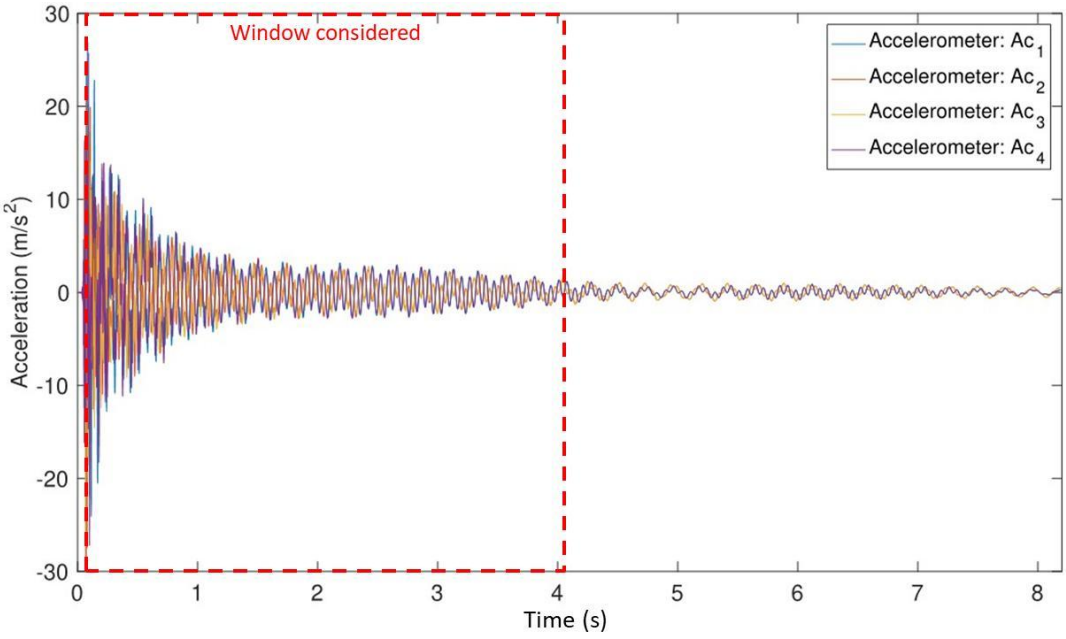

Figure 6 - Typical signal sample of 2-story laboratory frame. Adapted from Finotti et al. (2023) [48].

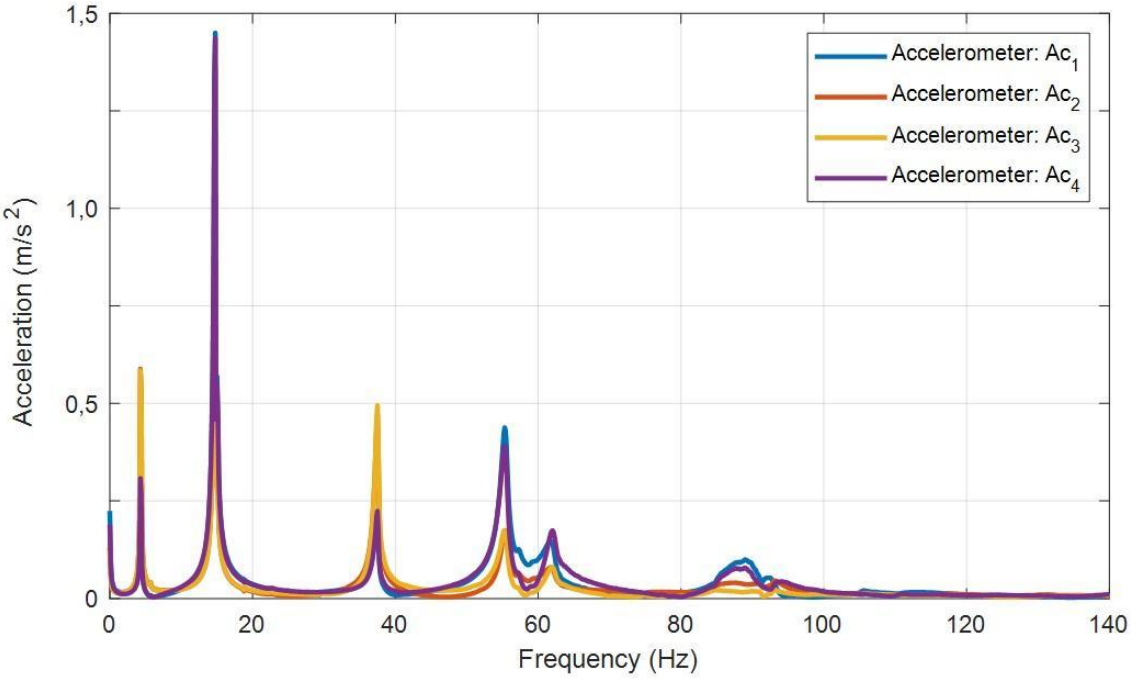

Figure 7 - Frequency response of the 2-story laboratory frame [48].

4.1.1) Results and discussion

As explained in Subsection 4.1, an anomaly is introduced by placing a mass at the center of the second floor, positioned between sensors #2 and #3. Therefore, for analytical purposes,

these sensors are the ones more prone to detect any potential structural damage. This is because perturbations in the structure's mass, stiffness, and energy dissipation properties are frequently related to damage [49]. The primary goal of this experiment is thus to examine the effectiveness of the proposed methodology's localization (Rytter scale level 2). The secondary objective is to assess its quantification (Rytter scale level 3), which concerns how consistently the indicators react to progressive damage scenarios.

For control, the quantum technique is applied using different numbers of qubits, specifically 1-qubit, 2-qubit and 3-qubit systems, and then compared with their classical counterparts. Configurations with more qubits were not considered due to computational time constraints. As for the classical methods, k-means and hierarchical clustering were chosen since both are well-established unsupervised classification techniques. Additionally, k-means was tested considering three different metrics: Euclidean, cityblock, and cosine [50]. As for the hierarchical clustering, four distinct linkage methods were used to determine the distance between clusters: single, complete, average and ward [50]. Notably, clustering methods require a minimum of two clusters for classification. In this case, one cluster represents the baseline intact scenario features, while the other captures the unknown scenario features. This process is performed independently for each examined scenario and for each sensor.

Moreover, theoretical concepts of binary classifications are explored and used to create a damage index from the models' accuracies. In this case, 100% of accuracy means that the data could be completely separated, leading to the hypothesis that there are different structural behaviors, which indicates a high potential for anomaly near a given sensor. Conversely, 50% of accuracy means that the data were randomly separated, thus, both healthy and damaged data were considered to display similar behaviors, *i.e.*, the algorithm failed to distinguish these datasets, which indicates low potential for anomaly.

Figures 8(a), (b), and (c) illustrate the clustering accuracies obtained for each sensor, considering different damage scenarios and clustering approaches. The red curve in Fig. 9 illustrates the expected behavior of the results, representing the optimal accuracy distribution among the sensors that best reflects the actual locations of the anomalies. This curve serves to provide a clear and objective depiction of method's capability for anomaly localization and quantification. In Fig. 9(a), the red curve is a smooth, wavy line centered around 50%, representing the expected behavior in an intact scenario. In Fig. 9(b), the curve forms a

quadratic parabola centered between sensors #2 and #3. A similar pattern is observed in Fig. 9(c), but with greater intensity due to the progression of damage. For the intact data, all models, both classical and quantum, yielded accuracies near the random threshold (50%), except for hierarchical clustering embedded, which all linkage scheme demonstrated false positives at sensor #3. It reflects the challenge of differentiating between baseline and other intact scenarios, where minimal structural variation is expected.

For damage scenario I, the proposed quantum approach successfully locates damage at sensor #2 for the case of 1 and 2 qubits (see Fig. 8(b)), while k-means pinpoints damage at sensor #3 and hierarchical indicates at sensor #2, both being acceptable responses (ground truth is #2 and #3). The latter showed a false positive (FP) at sensor #4 (ward linkage), but also achieved the highest accuracies. Quantitatively, for this 1-qubit case, the accuracy indices increased from new intact data to damage scenario I $\left(\frac{Acc_{Damage\ I}}{Acc_{New\ intact}} - 1\right)$ by +22.2%/**+41.5%**/-2.1%/+9.8% for each sensor, respectively. As for damage scenario II, the indices' increases $\left(\frac{Acc_{Damage\ II}}{Acc_{New\ intact}} - 1\right)$ were of +5.5%/**+64.2%**/-21.3%/-9.8%, respectively. Other ratios can be found in Table 4.

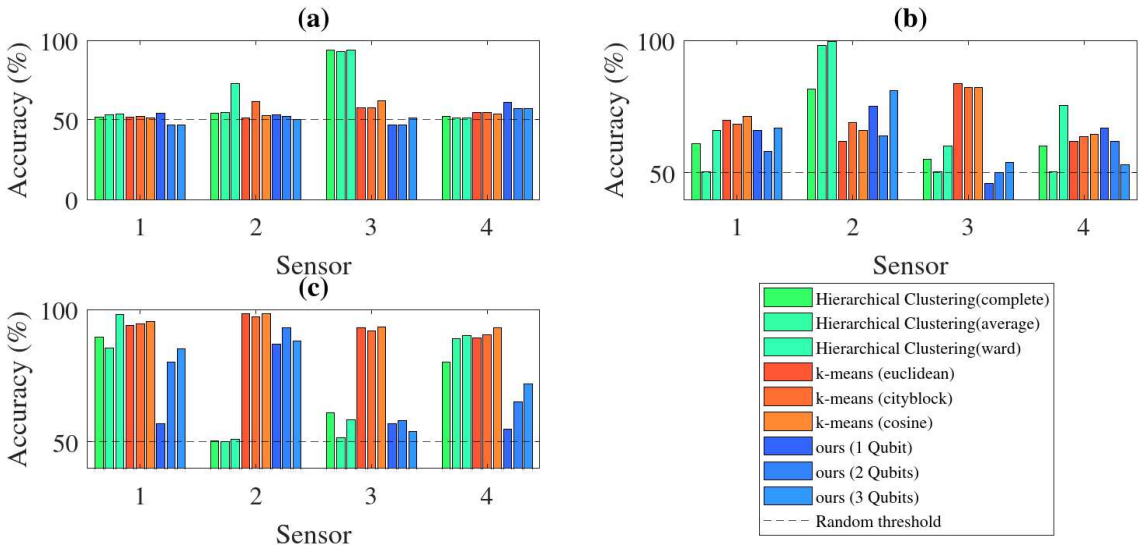

Figure 8 - Accuracy results for the laboratory 2-story frame: (a) New intact scenario, (b) Damage scenario I and (c) Damage scenario II.

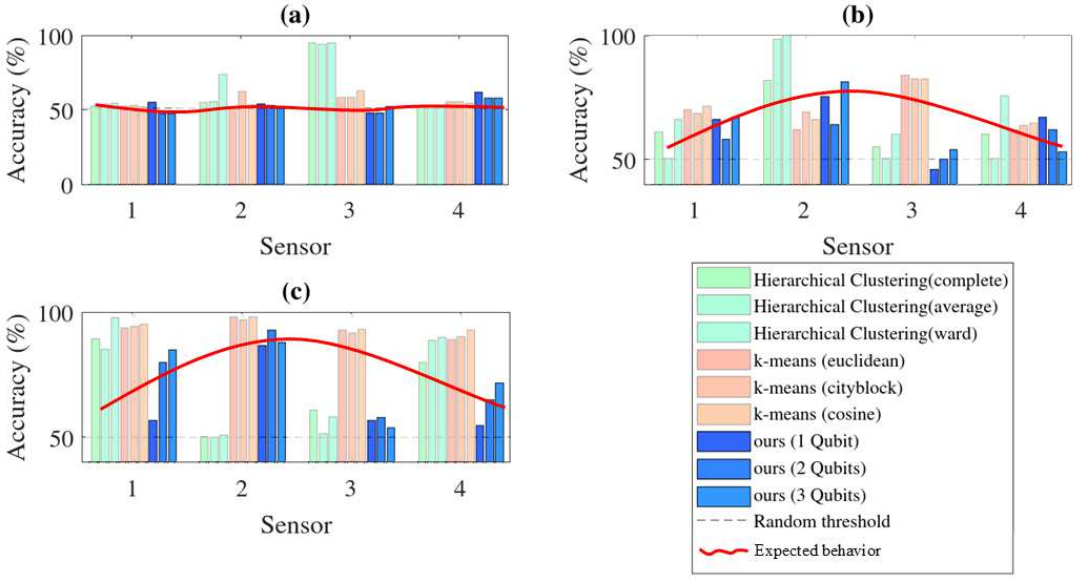

Figure 9 - Detailed analysis of results of laboratory 2-story frame: (a) New intact scenario, (b) Damage scenario I and (c) Damage scenario II

Table 4 – Ratio between accuracy results of two-story frame - Ratio A: $\frac{Acc_{Damage\ I}}{Acc_{New\ intact}} - 1$ and Ratio B: $\left(\frac{Acc_{Damage\ II}}{Acc_{New\ intact}} - 1\right)$.

Model	Ratio	Sensor #1	Sensor #2	Sensor #3	Sensor #4
Ours (1 qubit)	A	+22.2%	**+41.5%**	-2.1%	+9.8%
	B	+5.5%	**+64.2%**	-21.3%	-9.8%
Ours (2 qubit)	A	**+23.4%**	+23,1	+6.4%	+8.8%
	B	+70.2% *	**+78.8%**	+23.4%	+14.0%
Ours (3 qubit)	A	+42.6%	**+62.0%**	+5.9%	-7.0%
	B	**+80.9%** *	+76.0%	+5.9%	+26.3%
Hierarchical clustering (Complete)	A	+18.4%	**+50.9%**	-41.5%	+15.4%
	B	**+73.8%** *	-6.5%	-35.1%	+53.8% *
Hierarchical clustering (Average)	A	-4.7%	**+79.8%**	-45.7%	-1.0%
	B	**+61.3%** *	-8.2%	-44.6%	+74.5% *
Hierarchical clustering (Ward)	A	+23.4%	+36.3%	-36.2%	**+48.0%**
	B	**+83.2%** *	-30.1%	-37.8%	+76.5% *
K-means (Euclidean)	A	+34.7%	+21.2%	**+45.8%**	+13.8%
	B	+81.3% *	**+93.1%**	+62.2%	+63.8% *

K-means (Cityblock)	A	+31.5%	+12.4%	**+42.7%**	+16.7%
	B	**+81.7%** *	+58.3%	+59.7%	+66.1% *
K-means (Cosine)	A	**+38.6%**	+25.1%	+32.8%	+20.7%
	B	+85.9% *	**+86.8%**	+50.9%	+73.7% *

*Stands for excessive increase of false positives (values greater than +50,0%). **Bold** indicates the highest accuracy of each table line.

For damage scenario II, the QML method kept its indication of anomaly at sensor #2 and produced better outcomes when the number of qubits was set to one, as observed in Fig. 8(c). However, there are some issues about the reliability of the compared clustering methods. As damage severity increases from scenario I to II, the resolution of damage localization with k-means declines. As observed in Fig. 8(b-c), the increase of the local anomaly had a significant impact on the accuracy of the k-means model across all sensors. It shows high FPs in sensors #1 and #4 for all tested metrics. The hierarchical clustering failed completely at this scenario, misinterpreted the increase in mass, could not distinguish the new vibrational behavior at sensors #2-3 and shows excessive high FP at sensors #1 and #4. In other words, in this experiment, classical algorithms exhibited excessive sensitivity to structural changes, limiting the localization task in advanced damage stages. This is not ideal for sudden intense damage such as earthquakes, fires, or collisions [51]. However, it is still possible to accomplish the task of detecting the presence of damage (Rytter level I), which is indeed a less complex objective.

Regarding the secondary objective, the damage severity correlates with an increase in the accuracy of the proposed model. As seen in Fig.8(b-c), the QML approach consistently recognizes damage at sensor #2 and exhibits an increment in its indices, especially for the case of 1-qubit, where an increase of 16% was observed in sensor #2 indices from damage I to II, indicating a promising capability for quantification. Despite that, the accuracies of the 2-qubits and 3-qubits models exhibit a curve where the maximal peaks occur also at sensor #2, as observed in Fig. 8(c). Thus, the suggested quantum strategy performed better in terms of damage quantification at the local of damage than its classical counterparts.

Additionally, an increase in the number of qubits does not necessarily translate to a direct improvement in performance. This observation is reasonable given that an increase in the number of qubits entails a corresponding rise in complexity of the quantum circuit, leading to

more parameters to be trained. Consequently, this bigger complexity demands a larger volume of data to effectively train the quantum algorithm and return improved results.

In summary, regardless of variations in terms of performance across all scenarios and sensors, the quantum approach consistently proves itself competitive (Healthy scenario; Damage scenario I) or superior performance (Damage scenario II) compared to k-means and hierarchical clustering. This finding suggests that quantum-based approaches may be able to improve SHM capabilities, particularly in scenarios where traditional methods may fall short. It is important to note that quantum algorithms are still in their first phase of exploration compared to conventional ML, and achieving better or even comparable results to classical ML represents a promising advancement.

4.2) KW51 Railway Bridge

The steel railway bridge known as KW51 (see Fig.10(a)) is in Leuven, Belgium. Positioned along the railway line L36N between Leuven and Brussels, it spans over the Leuven–Mechelen canal. This bow-string type bridge is 115 meters long and 12.4 meters wide [52]. It is close to Leuven and Herent's railway stations, approximately 2.2 km and 2.3 km away, respectively, as shown in Fig.10(b). The bridge accommodates two ballasted electrified tracks, named track A on the north side and track B on the south side, with a maximum speed limit of 160 km/h. Both tracks have curved sections, with track A having a curve radius of 1,125 m and track B with a radius of 1,121 m. Opened for traffic in 2003, this bridge serves passenger trains traversing between Leuven and Brussels.

Figure 10 - (a) Photo of railway bridge KW51 in Leuven, Belgium, and (b) Schematic of its location [52].

The monitoring program began on October 2, 2018. Between May 15 and September 27, 2019, modifications were conducted to address a construction defect that was discovered during an inspection. The connections between the diagonals, arches, and bridge deck were strengthened due to these efforts. Images of these connections before and after retrofitting are shown in Fig.11(a) and Fig.11(b), respectively. Fig.11(c) displays the scaffolding that was employed during the strengthening procedure. Each diagonal had a steel box welded around its initially bolted connection where it intersected with the arches and deck. The acceleration measurements were collected over a 7.5-month period preceding retrofitting (October 2, 2018 – May 15, 2019), during the retrofitting phase (May 15 – September 27, 2019), and for 3.5 months post-retrofitting (September 27, 2019 – January 15, 2020) [52]. Hence, these three alterations in the bridge's dynamic behavior are treated in this section as structural "abnormalities" and are employed to validate the proposed methodology in real-world applications.

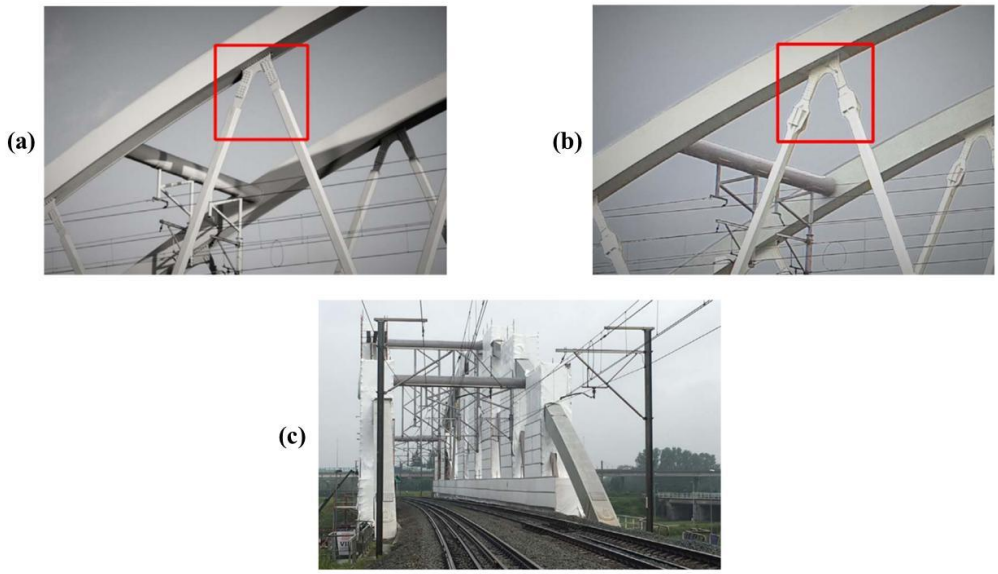

Figure 11 - Connections of KW51 bridge (a) before, (b) after and (c) during the retrofitting [52].

For this research, only six accelerometers (#1 to #6) (the ones mounted on the bridge deck, as shown in Fig. 12) were considered due to the less frequency of malfunctions during the monitoring (see Fig. 13). They correspond to those referenced in the report by Maes and Lombaert (2021) [52] as "aBD11Az", "aBD17Ay", "aBD17Az", "aBD17Cz", "aBD23Ay" and

“aBD23Az”, respectively. These are uniaxial sensors and the last letter of the nomenclature indicate the direction (y or z) where the measurements were recorded. Each accelerometer is placed inside an IP66-rated polycarbonate junction box, which is attached to the structure using a pot magnet [52]. Fig. 14 illustrates the sensor mounted on the structure. The time periods allocated for unsupervised training and testing are outlined in Fig. 13. Data for the *baseline*, *new intact*, *during retrofitting*, and *after retrofitting* scenarios were collected from the 1st to the 10th of March, April, July, and October of 2019, respectively. Each day within these periods, a 5-minute recording starting at 4 pm (defined by default) was captured at a sampling rate of 825.8 Hz. Subsequently, 10 samples, each lasting three seconds, were extracted from these original daily recordings, resulting in 100 signal samples for each scenario. An example of a typical dynamic response of the bridge is shown in Fig. 15. In addition, the average FFT both in z and y directions were computed and are displayed in Fig. 16(a) and Fig. 16(b), respectively.

Regarding environment factors, Fig. 17 presents the evolution of the surface temperature below the bridge deck and the air temperature at the Vliet Building in each scenario. The analysis reveals that the identified natural frequencies are influenced, to some extent, by temperature variations in certain modes, with a notable impact observed during the frost period in January 2019, which was not considered in this study. After the retrofitting, a small variation of the natural frequencies with respect to the situation before retrofitting is observed, owing to the presence of the scaffolding at both sides of the bridge [52], which corroborates the fact that retrofitting can induce detectable changes in the structure's vibrational behavior to validate the proposed model.

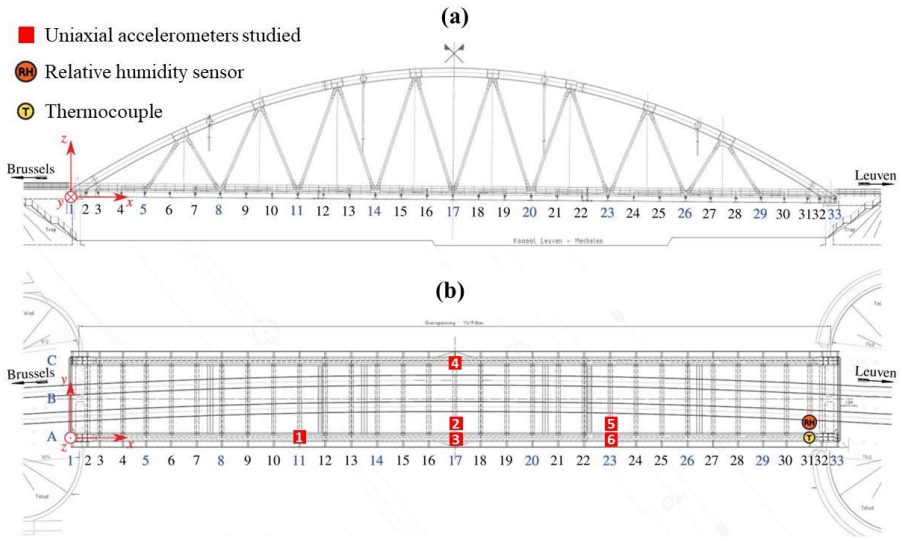

Figure 12 - KW51 bridge (a) lateral view; (b) studied accelerometers setup installed on the bridge deck. Adapted from Maes and Lombaert (2021)[52].

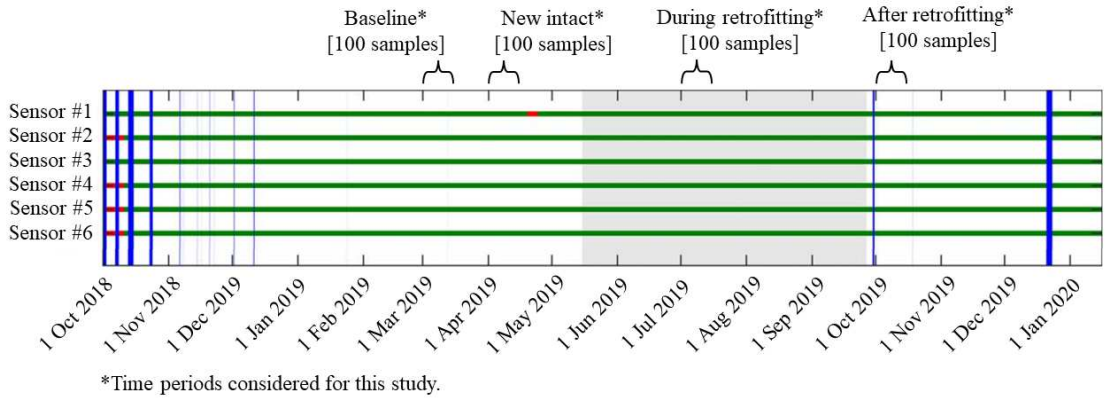

Figure 13 - Gantt Chart of Sensor Operations: Normal (green), Malfunction (red), Interruption (blue), and Retrofitting period (shaded gray). Adapted from Maes and Lombaert (2021) [52].

Figure 14 - (a) Accelerometers aBD17Az and aBD17Ay; and (b) accelerometer aAR1516Cy. [52].

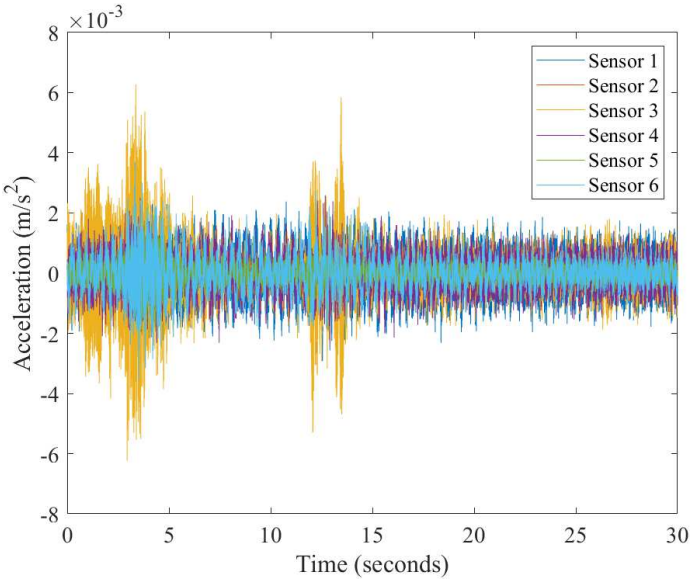

Figure 15 - Typical signals from the KW51 Railway Bridge on March 1st, 2019, at 4:00 AM

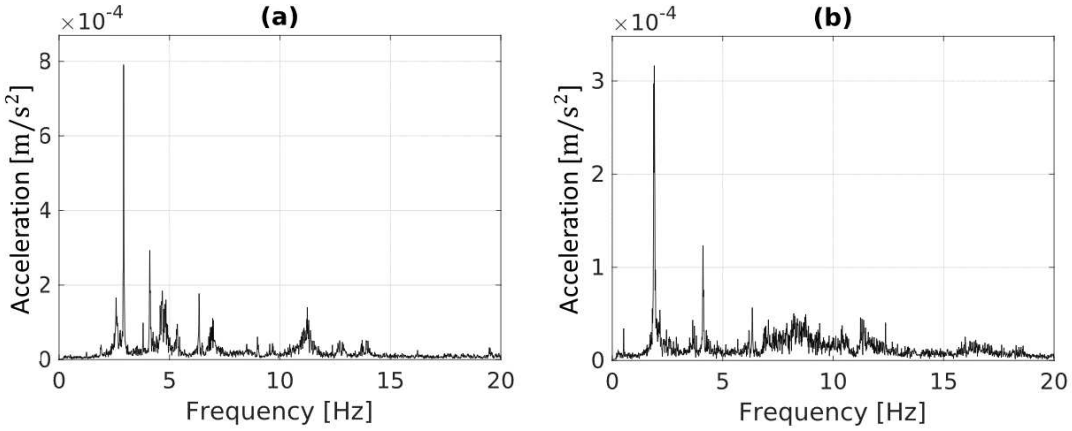

Figure 16 - Mean frequency in (a) Z-direction and (b) Y-direction from the KW51 Railway Bridge on March 1st, 2019, at 4:00 AM

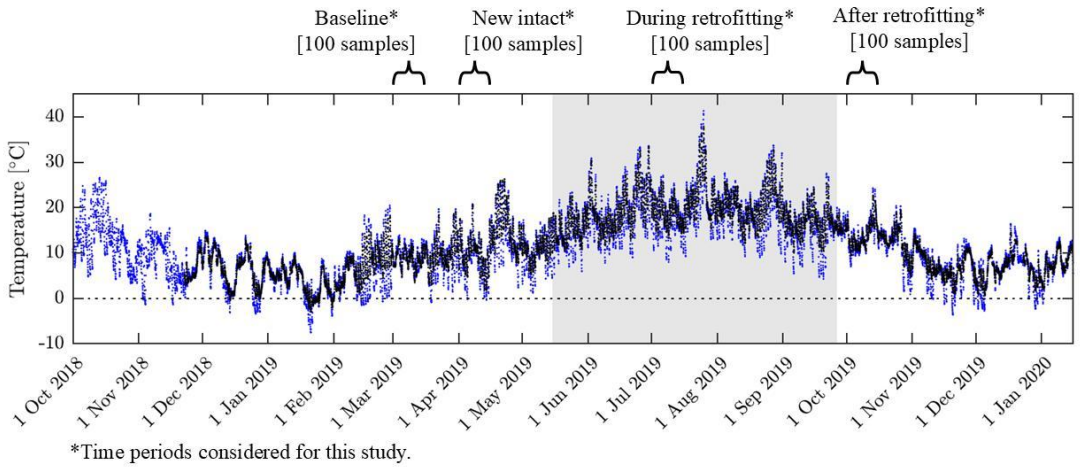

Figure 17 - Time history of the surface temperature below the bridge deck (black); the air temperature at the Vliet Building (blue) and Retrofitting period (shaded gray). Adapted from the study of Maes and Lombaert (2021) [52].

4.2.1) Results and discussion

This experiment stands out as the most complex for this study since it incorporates a variety of environmental parameters and takes place under real operational and ambient conditions. The tests consist in simulating structural anomaly in the bridge connections, which could be potentially resulted from factors like overloading due to poor design/construction, material fatigue, seismic activity, and corrosion [53, 54]. According to the work of Chmielewski and Muzolf (2023) [53], the damage by fatigue in railway bridge rates is greatly impacted by the

dynamic effects of freight rolling stock, especially with heavy freight transport. Moreover, the degradation of these structures resulting from track misalignment is also considerable.

The introduced anomaly impacts the structural dynamics of the entire bridge due to the reinforced connections across its span, as seen in Fig.11. Consequently, all six accelerometers are prone to measure signs of damage (Rytter scale level 1 - detection). The main goal of this application is to examine whether the sensors display higher indices more frequently during abnormal conditions compared to the intact state. Additionally, the secondary objective is to verify the potential for quantifying the level of damage.

Like the application discussed in Subsection 4.1, the proposed method is compared with two classical algorithms, k-means and agglomerative hierarchical clustering, using multiple parameters. The performance index in Fig. 18 is determined by the accuracy of correctly distinguishing the unknown data from the known intact scenario data. A classification accuracy of 100% indicates perfect classification, while 50% suggests random classification. As in the first application, the red curve in Fig. 19 represents the expected behavior of the results, illustrating the ideal accuracy distribution among the sensors that best aligns with the actual anomaly locations. In Fig. 19(a), the red line appears as a smooth, wavy curve centered around 50%, reflecting the expected behavior in an undamaged scenario. In Fig. 19(b), this curve is expected to move upward, indicating a deviation from the intact state. In Fig. 19(c), further upward movement or an increase in the number of bars reaching higher values is expected, corresponding to the progression of damage.

When examining the first objective, the quantum approach performs better with the new intact scenarios by revealing less events of false positives, as shown in Fig. 18(a). The 1-qubit model shows two FPs (sensors #4 and #6), while the 2-qubits and 3-qubits models only have one false positive in sensor #6, with the remaining sensors hovering around 50% accuracy (<5% variation). In contrast, the k-means algorithm yields high indices across all sensors, incorrectly identifying differences in bridge integrity between March and April 2019, leading to maximum false positives. Additionally, the 20-day monitoring window is too short for actual degradation to occur, highlighting the ineffectiveness of the classical approach in this context. The hierarchical clustering also shows FPs at all sensors with most linkage methods except for *average* variant. (*complete:* FPs at #2, #5 and #6 sensors; *ward*: FPs at all sensors). This could

be caused by external noise, such as an unusually windy month, in which the classic algorithms misinterpreted as a novel structural dynamic pattern.

During the retrofitting period, as depicted in Fig. 18(b), the k-means algorithm consistently maintains high indices; however, these values remain stable compared to the previous phase, as observed in Table 5. Hierarchical clustering similarly indicates damage across all sensors with a slight increase from the prior scenario, particularly for sensors #1, #2, and #3. Thus, for the classic algorithms, since they have detected anomaly in the intact structure incorrectly, the actual indications in this new vibrational behavior do not contribute significatively for the overall quality of the results obtained and suggests a lack of robustness. In contrast, QML unsupervised classifier identifies damage in two sensors (#2 and #4) with the 1-qubit setting, one sensor (#6) with the 2-qubit system, and three sensors (#2, #5 and #6) with 3-qubit. Quantitatively, for this 1-qubit case, the accuracy indices increased from the new intact data scenario during the retrofitting phase $\left(\frac{Acc_{During}}{Acc_{New\ intact}} - 1\right)$ by -7.4%/**37.5%**/4.2%/**17.5%**/0/-34.1% for each sensor, respectively. Conversely, after the retrofitting (Fig. 18(c)), these increases $\left(\frac{Acc_{After}}{Acc_{New\ intact}} - 1\right)$ were observed as -5.6%/**51.8%**/4.2%/**30.2%**/**72.0%**/-1.2%, respectively. Additional ratios can be found in Table 5.

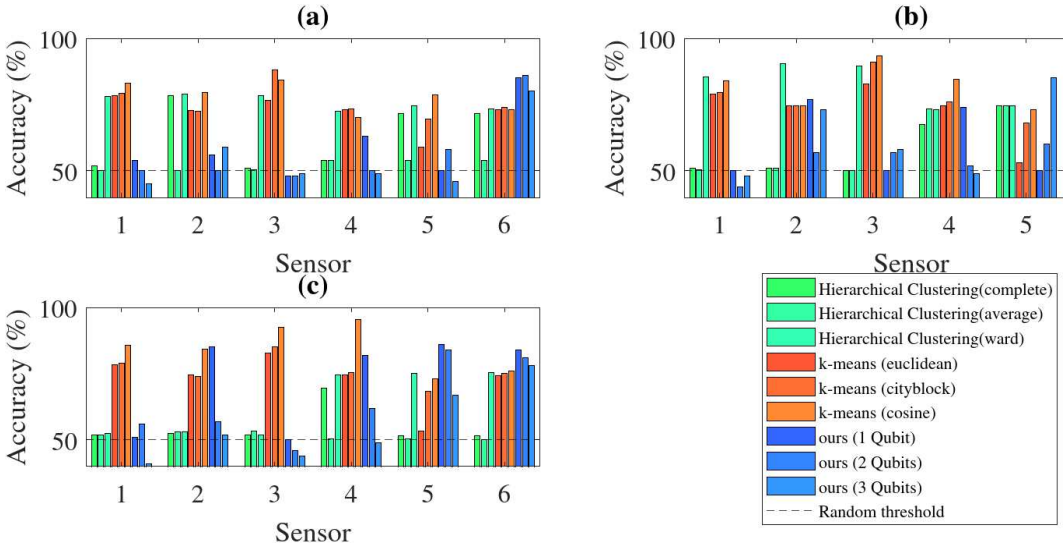

Figure 18 - Accuracy results for the KW51 railway bridge: (a) Before retrofitting, (b) During retrofitting and (c) After retrofitting.

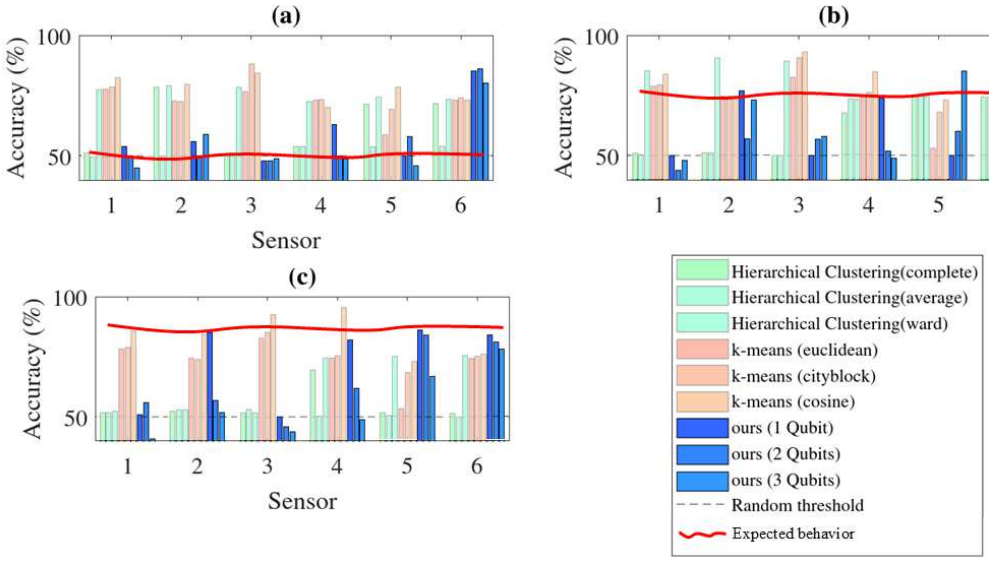

Figure 19 - Detailed analysis of results of KW51 railway bridge: (a) Before retrofitting, (b) During retrofitting and (c) After retrofitting.

Table 5 - Ratio between accuracy results of KW-51 bridge - Ratio A: $\frac{Acc_{During}}{Acc_{New\ intact}} - 1$ and Ratio B: $\left(\frac{Acc_{After}}{Acc_{New\ intact}} - 1\right)$.

Model	Ratio	Sensor #1	Sensor #2	Sensor #3	Sensor #4	Sensor #5	Sensor #6
Ours (1 qubit)	A	-7.4%	**+37.5%**	+4.2%	**+17.5%**	0	-34.1%
	B	-5.6%	**+51.8%**	+4.2%	**+30.2%**	**+72.0%**	-1.2%
Ours (2 qubit)	A	-12.0%	+14.0%	**+18.8%**	+4.0%	+3.5%	-18.6%
	B	+12.0%	+14.0%	-4.2%	**+24.0%**	**+44.8%**	-5.8%
Ours (3 qubit)	A	+6.7%	**+23.7%**	**+18.4%**	0	**+84.8%**	-11.2%
	B	-8.9%	-11.9%	-10.2%	0	**+45.7%**	-2.5%
Hierarchical clustering (Complete)	A	-1.9%	-35.0%	-2.0%	**+25.0%**	+4.2%	+4.2%
	B	0	-33.1%	+2.0%	**+28.7%**	-28.0%	-28.0%
Hierarchical clustering (Average)	A	+1.0%	+2.0%	-1.0%	**+36.1%**	**+38.0%**	**+38.0%**
	B	+4.0%	+6.0%	+5.9%	-6.5%	-6.5%	-7.4%
Hierarchical clustering (Ward)	A	+9.6%	+14.6%	+14.0%	+0.7%	0	+1.4%
	B	-32.7%	-32.9%	-33.8%	+2.8%	+0.7%	+2.7%
K-means (Euclidean)	A	+0.6%	+2.3%	+8.1%	+1.8%	-10.3%	+1.4%
	B	0	+2.4%	+8.3%	+1.8%	-9.5%	+1.7%
K-means (Cityblock)	A	+0.4%	+2.8%	+3.4%	+3.4%	-2.2%	+0.7%
	B	-0.2%	+2.1%	-3.1%	+2.7%	-0.6%	+1.4%
K-means (Cosine)	A	+1.2%	-6.4%	+10.6%	**+20.9%**	-7.1%	+2.7%
	B	+3.3%	+5.7%	+9.7%	**+36.3%**	-6.9%	+4.3%

Note: **Bold** stands for a significant increase in accuracy.

In the period after the retrofitting, shown in Fig. 18(c), the QML approach identifies damage in four out of the six sensors (#2, #4, #5, #6) with high indices for the 1-qubit case, and in two sensors (#5 and #6) for the 2-qubit and 3-qubit cases. This increase in damage alarms corresponds to the escalation of actual damage. In fact, the changes in stiffness due to joint reinforcement are more pronounced in this last scenario. Consequently, the detection becomes more precise as abnormalities deviate further from the baseline condition. On the other hand, the performance of the k-means remains unchanged from the previous monitoring phases. The hierarchical algorithm maintained or decreased accuracy as damage increased.

As for the secondary objective, it is evident that the QML approach exhibits greater potential for damage quantification. The correlation between the number of high-index accuracies and the increase of structural anomalies highlights this capability. Again, the increase in the number of qubits did not necessarily translate to a direct improvement in performance. This is because the rise in complexity was not accompanied by additional data for fine-tuning. Both experiments explored in this paper used the same number of training samples.

In summary, the proposed approach demonstrates a reasonable ability to detect changes in structural integrity, such as structural reinforcement in a real-scale bridge and outperformed the classical technique's performances.

5) Limitations and considerations

Like with any other data-driven damage localization method, the efficiency of the proposed approach is inherently influenced by both the number and arrangement of the sensors. Insufficient sensor coverage or improper sensor placement can lead to gaps in data collection, limiting the methodology's ability to detect and pinpoint damage accurately. Careful consideration should be given to sensor deployment strategies, including the selection of sensor types, cost, positioning, and the overall sensor network design. By optimizing these elements, SHM procedures can achieve their maximal effectiveness [55].

Another issue is the induced anomalies, which are simulated by adding mass in the case of the two-story frame and increasing stiffness in the case of the K51 bridge. While this may not

perfectly replicate true damage behavior, it is considered a reasonable structural abnormality to be investigated since changes in these parameters are usually associated with deterioration [49].

Moreover, while environmental and operational variability (*e.g.*, temperature fluctuations, wind loads) are naturally embedded in the collected signals, their explicit impact on the performance of the proposed approach has not been isolated or extensively analyzed. The methodology relies on preprocessing techniques, such as feature normalization and dimensionality reduction, to mitigate the effects of these external factors. However, future studies are recommended to further investigate the robustness of the approach under extreme noise scenarios to better understand its practical applicability in real-world SHM settings.

As with any ML application, ensuring the model's generalizability to different structures remains a challenge. The proposed QML technique has shown promising results in two independent case studies: a laboratory frame and a full-scale bridge, suggesting potential for generalization. Notably, since the model is trained exclusively on baseline structural vibration data (*e.g.*, intact, actual, or lightly damaged), regardless of geometry or material properties, it may be seamlessly applicable to a wide range of structures without requiring any prior knowledge about them. However, its performance across various structural configurations, particularly in situ or open-field circumstances, has not been comprehensively evaluated and should be considered for future research.

Data acquisition in practical settings can be significantly more complex than in controlled laboratory environments. Factors such as noise interference, sensor calibration issues, and variability due to environmental conditions can impact the quality of the acceleration signals, potentially affecting the accuracy of the anomaly detection process.

Another challenge is scalability. While the proposed approach demonstrated promising results on the KW51 bridge and a laboratory frame, scaling the QML framework to larger and more complex structures may require significant computational resources and preprocessing time. The average training time per sensor was 22.8 ± 1.1 min for the 1-qubit system, 51 ± 2.6 min for the 2-qubit system, and 124 ± 19.0 min for the 3-qubit system. These values were consistent across both applications, as they employed identical numbers of features, samples, and scenarios.

Furthermore, an important limitation of our study lies in the fact that the quantum circuit is simulated on a classical computer. This means that the presence of noise and errors inherent to real-world quantum machines were not considered. It is known that quantum states are very sensitive to environmental disturbances, such as fluctuations in temperature, electromagnetic fields and mechanical vibrations [56]. When these systems interact with an external environment, the overall effect reduces the purity of the qubits through a phenomenon known as decoherence [34], which contracts the vector associated with the respective wave function in the Bloch sphere (Fig. 1) towards its center.

In addition, NISQ devices are also susceptible to noise sources related to circuit depth and width [57], which determine its spatial and temporal complexities and the success rate of the algorithm. These errors increase by scaling the number of qubits and the interconnectivity between them [35], as well as the execution time of the logic gates and the amount of information processed through the controlled operations $U(x)$ and $V(\alpha, \gamma)$ [58]. For these reasons, surpassing noise sources is one of the biggest challenges in the field of Quantum Computing.

Without taking these factors into account, the results obtained by the proposed approach may be somewhat worse when compared to those that may be achieved in an ideal quantum computer with more qubits. In fact, Quantum Computing technology is still in its emerging stages, and widespread adoption may require significant advancements in hardware development and infrastructure.

To take into consideration all these constraints, we propose exploring hybrid quantum-classical algorithms as a potential solution to current limitations in quantum hardware, particularly regarding scalability and error rates. Further, we recognize the need for validation of the framework on a broader range of structures and operating conditions to enhance its generalizability. Finally, integrating domain-specific knowledge, such as physics-based models, into the QML approach could improve the interpretability and robustness of the results, spreading its application in practical engineering scenarios.

It is important to acknowledge these limitations and recognize that further research and experimentation are necessary to fully understand the capabilities of Quantum Computing in SHM applications.

6) Concluding remarks and future work

This paper intended to show the capabilities of unsupervised QML for vibration-based structural health monitoring. The methodology consisted in extracting eleven statistical features from the time domain and encoding them into quantum states for analysis using a quantum classifier. The model was trained using known healthy data and an anomaly score function was optimized to detect deviations from normal vibrational behavior, thereby detecting potential further structural anomalies in an unsupervised manner. The proposed method showed promising results in damage assessment tasks in both applications evaluated: a two-story slender laboratory frame and a real-scale railway bridge. The paper's key findings and implications are summarized below:

- The statistical feature extraction and min-max normalization conducted to preprocess the raw data obtained from the sensors proved effective in standardizing the data for input into the algorithm.
- In the laboratory application, the proposed method performed better than classic ML approaches when faced with new intact data, with minor observed variations (<5%) around the threshold for random classification.
    - The quantum approach demonstrated superior localization capabilities, particularly in advanced damage stages, as it achieved higher accuracy in pinpointing the location of damage within the structure. Conversely, the k-means and hierarchical clustering method exhibited notable false positives in this regard.
    - Overall, the QML strategy demonstrates superior quantification capabilities, particularly when utilizing one qubit.
- For the case of the railway bridge, variations in environmental conditions, such as wind and temperature, were observed to have minimal impact on the accuracy of the damage localization analysis.
    - The method was able to detect different degrees of structural reinforcement in the real scale bridge.
    - The increase in the number of qubits did not necessarily result in improved performance in both applications, as it necessitates more data to effectively train the circuit parameters. This is evident as both applications were evaluated using

the same amount of data, which might not have been sufficient to fully leverage the increased qubit count.

In conclusion, the quantum approach consistently competed or outperformed the classical clustering one, highlighting its application to SHM problems. As quantum hardware technology continues to advance and become more accessible, the potential for QML algorithms to evolve in complexity and capability grows. This progression may lead to QML models outperforming classic ML ones in various applications. In the authors' perspective, despite being relatively new, QML in real-world applications offers the SHM industry significant insights into how it can be utilized and opens the way for further study directions in the topic.

In particular, expanding the number of qubits and logical operations required to execute the algorithm respectively increases the width and depth of the circuit. Consequently, it is expected that the decoherence process tends to be significative in real experiments, corrupting data and intensifying the overall error rates associated with logic gates. For future works, it is recommended to test other circuit architectures, examine other quantum encoding schemes, investigate quantum error correction protocols and compare the influence of noise levels on the results extracted from real quantum computers with those obtained in the simulator device used in this study. Furthermore, the exploration of alternative features and extraction processes are encouraged. For example, the implementation of an autoencoder could automate the feature computation process instead of relying on handcrafted features.

Data availability statement

For the two-story slender aluminum frame, the dataset is described in the work of Finotti *et al.* (2023). Those interested in accessing this dataset can find it at the SHM-UFJF repository via the following link: http://bit.ly/SHM-UFJF. Similarly, the dataset relating to the KW51 railway bridge is detailed in the study conducted by Maes and Lombaert (2021) and available for access through an online repository using the following DOI:10.5281/zenodo.3745914.

Code availability

The code used in this work can be found at this GitHub repository: https://github.com/cidengcnpq/qml.git

Acknowledgements

This study was partly funded by CAPES (Finance Code 0001), Conselho Nacional de Desenvolvimento Científico e Tecnológico - CNPq (Brazil) - Grants 303982/2022-5 and 402533/2023-2, FAPEMIG (Fundação de Amparo à Pesquisa do Estado de Minas Gerais – Grant APQ-00032-24).

7) References

[1] PCA (Portland Cement Association), **Types and causes of concrete deterioration**. IS 536.01, Glenview, IL, 2002.

[2] F. Biondini, D. M. Frangopol, 2016. Life-Cycle Performance of Deteriorating Structural Systems under Uncertainty: Review. **Journal of Structural Engineering**, 142(9), F4016001. https://doi.org/10.1061/(asce)st.1943-541x.0001544.

[3] A. Rytter, **Vibrational based inspection of civil engineering structures**. Dept. of Building Technology and Structural Engineering, Aalborg University, Fracture and Dynamics. R9314 (44), 1993.

[4] W. Tian, X. Cheng, Q. Liu, C. Yu, F. Gao, Y. Chi, 2021. Meso-structure segmentation of concrete CT image based on mask and regional convolution neural network. **Materials & Design**, 208, 109919. https://doi.org/10.1016/j.matdes.2021.109919.

[5] K. Kauss, V. Alves, F. Barbosa, A. Cury, 2024. Semi-supervised structural damage assessment via autoregressive models and evolutionary optimization. **Structures**, 59, 105762. Elsevier. https://doi.org/10.1016/j.istruc.2023.105762.

[6] Z. Daneshjoo, M. M. Shokrieh, M. Fakoor, 2018. A micromechanical model for prediction of mixed mode I/II delamination of laminated composites considering fiber bridging effects. **Theoretical and Applied Fracture Mechanics**, 94, 46–56. https://doi.org/10.1016/j.tafmec.2017.12.002.

[7] D. M. Frangopol, M. Liu, 2007. Maintenance and management of civil infrastructure based on condition, safety, optimization, and life-cycle cost. **Structure and Infrastructure Engineering**, 3(1), 29–41. https://doi.org/10.1080/15732470500253164.

[8] Y. Yang, M. Chadha, Z. Hu, M. D. Todd, 2022. An optimal sensor placement design framework for structural health monitoring using Bayes risk. **Mechanical Systems and Signal Processing**, 168, 108618. https://doi.org/10.1016/j.ymssp.2021.108618.

[9] M. Flah, I. Nunez, W. Ben Chaabene, M. L. Nehdi, 2021. Machine learning algorithms in civil structural health monitoring: a systematic review. **Archives of computational methods in engineering**, 28(4), 2621-2643. https://doi.org/10.1007/s11831-020-09471-9.

[10] A. Cury, D. Ribeiro, F. Ubertini, M. D. Todd, **Structural health monitoring based on data science techniques**, Springer, 2022. https://doi.org/10.1007/978-3-030-81716-9.

[11] H. B. Bisheh, G. G. Amiri, 2023. Structural damage detection based on variational mode decomposition and kernel PCA-based support vector machine. **Engineering Structures**, 278, 115565. Https://doi.org/10.1016/j.engstruct.2022.115565.

[12] Z., Chen, Y. Wang, J. Wu, C. Deng, K. Hu, 2021. Sensor data-driven structural damage detection based on deep convolutional neural networks and continuous wavelet transform. **Applied Intelligence**, 51(8), 5598-5609. https://doi.org/10.1007/s10489-020-02092-6.

[13] O. Abdeljaber, O. Avci, S., Kiranyaz, M. Gabbouj, D. J. Inman, 2017. Real-time vibration-based structural damage detection using one-dimensional convolutional neural networks. **Journal of sound and vibration**, 388, 154-170. https://doi.org/10.1016/j.jsv.2016.10.043.

[14] E. Figueiredo, G. Park, J. Figueiras, C. Farrar, K. Worden, 2009. **Structural health monitoring algorithm comparisons using standard data sets** (No. LA-14393). Los Alamos National Lab.(LANL), Los Alamos, NM (United States). https://doi.org/10.2172/961604.

[15] S. Sony, S. Gamage, A. Sadhu, J. Samarabandu, 2022. Vibration-based multiclass damage detection and localization using long short-term memory networks. **Structures**, 35, 436-451. Elsevier. Https://doi.org/10.1016/j.istruc.2021.10.088.

[16] M. Civera, V. Mugnaini, L. Zanotti Fragonara, 2022. Machine learning-based automatic operational modal analysis: A structural health monitoring application to masonry arch bridges. **Structural Control and Health Monitoring**, 29(10), e3028. https://doi.org/10.1002/stc.3028.

[17] D. Martucci, M. Civera, C. Surace, 2023. Bridge monitoring: Application of the extreme function theory for damage detection on the I-40 case study. **Engineering Structures**, 279, 115573. https://doi.org/10.1016/j.engstruct.2022.115573.

[18] Q. Zhang, K. Barri, S. K. Babanajad, A. H. Alavi, 2021. Real-time detection of cracks on concrete bridge decks using deep learning in the frequency domain. **Engineering**, 7(12), 1786-1796. https://doi.org/10.1016/j.eng.2020.07.026.

[19] S. Zhao, F. Kang, J. Li, 2022. Concrete dam damage detection and localisation based on YOLOv5s-HSC and photogrammetric 3D reconstruction. **Automation in Construction**, 143, 104555. https://doi.org/10.1016/j.autcon.2022.104555.

[20] J. Biamonte, P. Wittek, N. Pancotti, P. Rebentrost, N. Wiebe, S. Lloyd, 2017. **Quantum machine learning**. Nature, 549(7671), 195-202. https://doi.org/10.1038/nature23474.

[21] T. Hur, L. Kim, D. K. Park, 2022. Quantum convolutional neural network for classical data classification. **Quantum Machine Intelligence**, 4(1), 3. https://doi.org/10.1007/s42484-021-00061-x.

[22] D. Arthur, 2022. **A hybrid quantum-classical neural network architecture for binary classification**. arXiv preprint arXiv:2201.01820.

[23] C. H. H. Yang, J. Qi, S. Y. C. Chen, P. Y. Chen, S. M. Siniscalchi, X. Ma, C. H. Lee, 2021. Decentralizing feature extraction with quantum convolutional neural network for automatic speech recognition. In ICASSP **2021-2021 IEEE International Conference on Acoustics, Speech and Signal Processing (ICASSP)** (pp. 6523-6527). IEEE. https://doi.org/10.1109/ICASSP39728.2021.9413453.

[24] S. Wei, Y. Chen, Z. Zhou, G. Long, 2022. A quantum convolutional neural network on NISQ devices. **AAPPS Bulletin**, 32, 1-11. https://doi.org/10.1007/s43673-021-00030-3.

[25] Y. Trochun, Z. Wang, O. Rokovyi, G. Peng, O. Alienin, G. Lai, Y. Gordienko, S. Stirenko, 2021. Hurricane damage detection by classic and hybrid classic-quantum neural networks. In **2021 International Conference on Space-Air-Ground Computing (SAGC)** (pp. 152-156). IEEE. https://doi.org/10.1109/SAGC52752.2021.00033.

[26] C. Correa-Jullian, S. Cofre-Martel, G. San Martin, E. Lopez Droguett, G. de Novaes Pires Leite, A. Costa, 2022. Exploring Quantum Machine Learning and feature reduction techniques for wind turbine pitch fault detection. **Energies**, 15(8), 2792. https://doi.org/10.3390/en15082792.

[27] S. Bhatta, J. Dang, 2024a. Multiclass seismic damage detection of buildings using quantum convolutional neural network. **Computer-Aided Civil and Infrastructure Engineering**, 39(3), 406-423. https://doi.org/10.1111/mice.13084.

[28] S. Bhatta, J. Dang, 2024b. Quantum-enhanced machine learning technique for rapid post-earthquake assessment of building safety. **Computer-Aided Civil and Infrastructure Engineering**, vol 39, pp. 3188-3205. https://doi.org/10.1111/mice.13291.

[29] E. Bernstein, U. Vazirani, 1993. Quantum complexity theory. In **Proceedings of the twenty-fifth annual ACM symposium on Theory of computing** (pp. 11-20).

[30] U. Vazirani, 2002. A survey of quantum complexity theory. In **Proceedings of Symposia in Applied Mathematics** (Vol. 58, pp. 193-220).

[31] P. Kaye, R. Laflamme, M. Mosca, **An introduction to quantum computing**. OUP Oxford, 2006.

[32] N. D. Mermin, **Quantum Computer Science: An Introduction**, Cambridge University Press, New York, NY, USA, 2007.

[33] Z. Meglicki, **Quantum Computing Without Magic: Devices**, The MIT Press, Cambridge, MA, USA, 2008.

[34] G. Benenti, G. Casati, G. Strini, **Principles of Quantum Computation and Information: Basic Tools and Special Topics**, World Scientific Publishing Co., Inc., River Edge, NJ, USA, 2007.

[35] A. Javadi-Abhari, M. Treinish, K. Krsulich, C. Wood, J. Lishman, J. Gacon, S. Martiel, P. Nation, L. Bishop, A. Cross. B. Johnson, J. Gambetta, 2024. **Quantum computing with Qiskit**. arXiv preprint arXiv:2405.08810.

[36] M. Khan, M. Aman, B. Sikdar, 2024. Beyond Bits: A Review of Quantum Embedding Techniques for Efficient Information Processing. **IEEE Access**. vol. 12, pp. 46118-46137, 2024, https://doi.org/10.1109/ACCESS.2024.3382150.

[37] R. LaRose, B. Coyle, 2020. Robust data encodings for quantum classifiers. **Physical Review A**, 102(3), 032420. https://doi.org/10.1103/PhysRevA.102.032420.

[38] Y. Wang, Y. Wang, C. Chen, R. Jiang, W. Huang, 2022. Development of variational quantum deep neural networks for image recognition. **Neurocomputing**, 501, 566-582. https://doi.org/10.1016/j.neucom.2022.06.010.

[39] V. Alves, A. Cury, 2023. An automated vibration-based structural damage localization strategy using filter-type feature selection. **Mechanical Systems and Signal Processing**, 190, 110145. https://doi.org/10.1016/j.ymssp.2023.110145.

[40] C. Farrar, K. Worden, 2012. Structural health monitoring: a machine learning perspective. **John Wiley & Sons**. https://doi.org/10.1002/9781118443118.

[41] W. Caesarendra, T. Tjahjowidodo, 2017. A review of feature extraction methods in vibration-based condition monitoring and its application for degradation trend estimation of low-speed slew bearing. **Machines**, 5(4), 21. https://doi.org/10.3390/machines5040021.

[42] J. A. Cariño-Corrales, J. J. Saucedo-Dorantes, D. Zurita-Millán, M. Delgado-Prieto, J. A. Ortega-Redondo, R. Alfredo Osornio-Rios, R. de Jesus Romero-Troncoso, 2016. Vibration-Based Adaptive Novelty Detection Method for Monitoring Faults in a Kinematic Chain. **Shock and vibration**, 2016(1), 2417856. https://doi.org/10.1155/2016/2417856.

[43] L. Nunes, R. Finotti, F. Barbosa, A. Cury, 2021. A hybrid learning strategy for structural damage detection. **Structural Health Monitoring**, 20(4), 2143-2160. https://doi.org/10.1177/1475921720966.

[44] V. Alves, A. Cury, 2021. A fast and efficient feature extraction methodology for structural damage localization based on raw acceleration measurements. **Structural Control and Health Monitoring**, 28(7), e2748. https://doi.org/10.1002/stc.2748.

[45] J. Baker, H. Horowitz, S. K. Radha, S. Fernandes, C. Jones, N. Noorani, V. Skavysh, P. Lamontangne, B. Sanders, 2022. **Quantum variational rewinding for time series anomaly detection**. arXiv preprint arXiv:2210.16438.

[46] J. Baker, S. Radha, **Quantum detection of time series anomalies**. Pennylane. https://pennylane.ai/qml/demos/tutorial_univariate_qvr/, 2023. (accessed in 29 of December of 2024).

[47] J. Preskill, 2018. Quantum computing in the NISQ era and beyond. **Quantum**, 2, 79. https://doi.org/10.22331/q-2018-08-06-79.

[48] R. Finotti, C. Silva, P. Oliveira, F. Barbosa, A. Cury, R. Silva, 2023. Novelty detection on a laboratory benchmark slender structure using an unsupervised deep learning algorithm. **Latin American Journal of Solids and Structures**, 20, e512. https://doi.org/10.1590/1679-78257591.

[49] N. Alkayem, M. Cao, M. Ragulskis, 2019. Damage localization in irregular shape structures using intelligent FE model updating approach with a new hybrid objective function and social swarm algorithm. **Applied Soft Computing**, 83, 105604. https://doi.org/10.1016/j.asoc.2019.105604.

[50] MathWorks. **MATLAB (Version 24.2.0 R2024b)**. https://www.mathworks.com/products/matlab.html, 2024. (accessed in 29 of December of 2024).

[51] D. Otter, R. Joy, M. Jones, L. Maal, 2012. Need for bridge monitoring systems to counter railroad bridge service interruptions. **Transportation research record**, 2313(1), 134-143. https://doi.org/10.3141/2313-15.

[52] K. Maes, G. Lombaert, 2021. Monitoring railway bridge KW51 before, during, and after retrofitting. **Journal of Bridge Engineering**, 26(3), 04721001. https://doi.org/10.1061/(ASCE)BE.1943-5592.0001668.

[53] R. Chmielewski, P. Muzolf, 2023. Analysis of degradation process of a railway steel bridge in the final period of its operation. **Structure and Infrastructure Engineering**, 19(4), 537-553. https://doi.org/10.1080/15732479.2021.1956550.

[54] N. Lu, H. Wang, J. Liu, Y. Luo, Y. Liu, 2024. Coupled propagation behavior of multiple fatigue cracks in welded joints of steel-bridge. **Journal of Constructional Steel Research**, 215, 108532. https://doi.org/10.1016/j.jcsr.2024.108532.

[55] W. Ostachowicz, R. Soman, P. Malinowski, 2019. Optimization of sensor placement for structural health monitoring: A review. **Structural Health Monitoring**, 18(3), 963-988. https://doi.org/10.1177/1475921719825601.

[56] S. Resch, U. Karpuzcu, 2021. Benchmarking quantum computers and the impact of quantum noise. **ACM Computing Surveys (CSUR)**, 54(7), 1-35. https://doi.org/10.1145/3464420.

[57] S. Glisic, B. Lorenzo, 2022. **Artificial Intelligence and Quantum Computing for Advanced Wireless Networks**, Wiley. https://doi.org/10.1002/9781119790327.

[58] E. Combarro, S. González-Castillo, 2023. **A Practical Guide to Quantum Machine Learning and Quantum Optimization: Hands-on Approach to Modern Quantum Algorithms**, Packt Publishing.

[59] V. Bergholm *et. al.*, 2018. **Pennylane: Automatic differentiation of hybrid quantum-classical computations**. arXiv preprint arXiv:1811.04968.

Appendix A: The Postulates of Quantum Mechanics.

A.I) Postulate I

The state S of a physical system is completely described by a unit vector $|\psi\rangle$ *that resides in the Hilbert space* H_s *associated with the system. This vector is known as state vector or wave function, whose temporal evolution is governed by the Schrödinger equation given by*

$$\mathbf{H}|\psi(t)\rangle = i\hbar\frac{\partial|\psi(t)\rangle}{\partial t}, \tag{A.1}$$

where $\boldsymbol{H}$ *is a self-adjoint operator that represents the Hamiltonian of the system and* $\hbar = h/2\pi$*, with* h *being the Planck's constant determined experimentally as* $h = 6.626 \approx 10^{-34} J.s.$

As Eq. (A.1) is a first-order linear differential equation, any linear combination of particular solutions is also a solution for the wave function. In this sense, the nature of $|\psi\rangle$ can be defined in a Hilbert space [31] in terms of discrete or continuous variables. For the first case, the wave function has finite dimension and the number of coordinates that define it is limited. For the second case, however, $|\psi\rangle$ is seen as a continuous function of specific parameters (like spatial coordinates in a three-dimensional system) and the Hilbert space assumes infinite dimension. Since the focus of the present work relies on the first case (that is, on systems with finite dimensions and well-defined coordinates), we will assume that our Hilbert space H_s is always bounded.

Let us show how to determine the wave function under these restrictions. Every quantum system is governed by an intrinsic dynamic that rules its behavior over time through the following equation [34]:

$$|\psi(t)\rangle = \mathbf{U}(\mathbf{t}, \mathbf{t_0})\ |\psi(t_0)\rangle, \tag{A.2}$$

where $\mathbf{U}(\mathbf{t}, \mathbf{t_0})$ is called the temporal evolution operator and $|\psi(t_0)\rangle$ is the state of the system at some instant $t_0 < t$. In general, it is necessary to have prior information regarding both of them to predict the dynamics of the wave function.

When **H** is independent of time, the solution to Eq. (A.1) is given by

$$|\psi(t)\rangle = e^{\frac{-i\mathbf{H}(t-t_0)}{\hbar}}|\psi(t_0)\rangle \equiv \sum_{n=0}^{\infty}\frac{1}{n!}\left(\frac{-i\ (t-t_0)}{\hbar}\right)^n \mathbf{H^n}|\psi(t_0)\rangle. \tag{A.3}$$

On the other hand, when the parameters implicit in the Hamiltonian depend on the time elapsed between t_0 and t, it is necessary to resort to other types of techniques to calculate $|\psi(t)\rangle$ (as obtaining approximations of the matrix **H** through methods like the expansion of functions in Taylor series, for example).

A.II) Postulate II

Each observable O is associated with a self-adjoint operator $\boldsymbol{O}$ that resides in a Hilbert space H_s. If a measurement of O is performed on a system, the only possible results will be equal to the eigenvalues λ_i of the operator $\boldsymbol{O}$ according to the relation

$$\mathbf{O}|u_i\rangle = \lambda_i\,|u_i\rangle, \tag{A.4}$$

where $|u_1\rangle, |u_2\rangle, |u_3\rangle$ ... is an orthonormal basis of eigenstates of $\boldsymbol{O}$. If the system state vector is expanded on this basis as

$$|\psi(t)\rangle = \sum_i C_i(t)\,|u_i\rangle, \tag{A.5}$$

the probability that λ_i is the result of a measurement of the observable $\boldsymbol{O}$ at an instant t is given by

$$p(\lambda_i|t) = |\langle u_i|\psi(t)\rangle|^2 = |C_i(t)|^2. \tag{A.6}$$

The unitarity of $|\psi\rangle$ imposed by Postulate I can now be understood. Note that the probability associated with the result of a measurement of **O** is related to the coefficient $C_i(t)$ (also called the probability amplitude). Hence, if we consider the set of all possible outcomes, the sum of the probabilities related to these events must necessarily be equal to one. Consequently, the condition

$$\big||\psi\rangle\big|^2 = \sum_i |C_i(t)|^2 = \sum_i p(\lambda_i|t) = 1 \tag{A.7}$$

must be satisfied. Therefore, if $|\psi(t)\rangle$ represents the state of a system, it is necessarily unitary. The values of observables predicted in measurements associated with quantum operators are analogous to the quantities described by classical dynamic variables [34], such as energy (associated to the Hamiltonian), position, linear and angular momentum, among others. In turn, the condition imposed by Postulate II and Eq. (A.4) - where **O** must be a self-adjoint operator -

guarantees that all eigenvalues λ_i associated with observables are represented by real numbers [32].

However, the measurement of eigenvalues follows a probabilistic distribution, and these cannot be confused with intrinsic parameters of the system: electric charge and mass, for example, are invariant in relation to the observation reference in non-relativistic situations. On the other hand, there are quantum observables (such as the spin **O** operator) that do not have classical analogues, which reinforces that Quantum Mechanics provides a more complete description of nature than Classical Mechanics.

We emphasize that when the Hamiltonian is independent of time, the solution to Eq. (A.1) is given by Eq. (A.3). As Postulate II states that the possible results associated with an operator are equivalent to their respective eigenvalues, we can simplify the analysis by expressing $|\psi(t)\rangle$ in terms of the eigenstates of **H**. In this sense, the eigenstates and eigenvalues of **H** can be denoted respectively by $|E_N\rangle$ and E_N, where N is the parameter that defines the energy E_N of the system [34]. Hence,

$$\mathbf{H}|N\rangle = E_N\,|N\rangle \text{ for } N \in \mathbb{N}. \tag{A.8}$$

By expanding the initial state of the wave function as

$$|\psi(t_0)\rangle = \sum_N C_N(t_0)|N\rangle \tag{A.9}$$

and subjecting it to the action of the operator **H**, we conclude that

$$|\psi(t)\rangle = e^{\frac{-i\mathbf{H}(t-t_0)}{\hbar}}|\psi(t_0)\rangle = \sum_{n=0}^{\infty} C_N \frac{1}{n!}\left(\frac{-i\,(t-t_0)}{\hbar}\right)^n \mathbf{H}^n|N\rangle = \tag{A.10}$$

$$\sum_{n=0}^{\infty} C_N \frac{1}{n!}\left(\frac{-i\,(t-t_0)}{\hbar}\right)^n (E_N)^n|N\rangle = \sum_N C_N(t_0)\, e^{\frac{-iE_N(t-t_0)}{\hbar}}|N\rangle.$$

Consequently, $|\psi(t)\rangle$ can be expressed as a function of the energy values E_N that satisfies Eqs. (A.2) and (A.8). For the particular case where the initial state coincides with one of the eigenstates of **H** such that $|\psi(t_0)\rangle = |N\rangle$, the final state of the wave function is given by

$$|\psi(t)\rangle = e^{\frac{-iE_N(t-t_0)}{\hbar}}|N\rangle. \tag{A.11}$$

Since $\left|e^{i\theta}\right| \equiv 1$ for any real parameter θ, the norm of $|\psi(t)\rangle$ is equivalent to

$$\left|\left|\psi(t)\right\rangle\right| = \left|e^{\frac{-iE_N(t-t_0)}{\hbar}}\right| x \left|\left|N\right\rangle\right| = \left|\left|N\right\rangle\right|. \tag{A.12}$$

The invariance of the norm of $|\psi(t)\rangle$ with respect to time in Eq. (A.12) implies that the transformation $\mathbf{U}(\mathbf{t}, \mathbf{t_0}) \propto \mathbf{I}$ is unitary, as shown in Eq. (3) and resumed in Eq. (21). Therefore, the probability $|C_N(t)|^2$ of the system being found in the stationary eigenstate $|N\rangle$ during the time interval elapsed between t_0 and t is constant. In this case, the analogy of the action of the operator **H** with the classical concept of energy conservation is valid, since any measurement on $|\psi(t)\rangle$ always reveals the same energy value E_N. Also note that systems that differ by a factor $e^{i\theta}$ are equivalent, since the predictions regarding the probabilities of collapse for a given state are identical for both. Thus, we say that two systems $|\psi(t)\rangle$ and $|\psi'(t)\rangle$ are similar if the only difference between them is a phase factor equal to $e^{i\theta}$, where θ is a parameter that can be associated with any real number.

Postulate III

When the measurement of an observable $\boldsymbol{O}$ *on a system initially described by the state vector* $|\psi(t)\rangle$ *provides the result* λ_i*, the state of this system is immediately described by*

$$\frac{\mathbf{P_i}\,|\psi(t)\rangle}{\sqrt{\langle\psi(t)|\mathbf{P_i}|\psi(t)\rangle}} \tag{A.13}$$

after carrying out this measurement, where $\boldsymbol{P_i} = |u_i\rangle\langle u_i|$ *is the projection operator relative to the subspace corresponding to* λ_i*.*

We start the analysis of the third Postulate considering that the eigenvalues λ_i of **O** are not degenerate and remembering that the expression $\mathbf{O}|u_i\rangle = \lambda_i\,|u_i\rangle$ is valid for any eigenstate $|u_i\rangle$ of **O**. Thus, when the measurement of this operator on the system provides the eigenvalue λ_i as a result, Eqs. (A.5) and (A.6) predict that the system will collapse to$|u_i\rangle$. If we compare this premise with Eq. (A.13), we will conclude that both are equivalent. Since λ_i is not degenerate, $|u_i\rangle$ will be the only state contained in the projector $\mathbf{P_i}$ associated with this eigenvalue. By replacing the term $\mathbf{P_i} = |u_i\rangle\langle u_i|$ in (A.13), we find that

$$\frac{\mathbf{P_i}\,|\psi(t)\rangle}{\sqrt{\langle\psi(t)|\mathbf{P_i}|\psi(t)\rangle}} = \frac{|u_i\rangle\langle u_i|\psi(t)\rangle}{\sqrt{\langle\psi(t)|u_i\rangle\langle u_i|\psi(t)\rangle}} = \frac{\langle u_i|\psi(t)\rangle|u_i\rangle}{\sqrt{|\langle u_i|\psi(t)\rangle|^2}} = e^{i\theta}|u_i\rangle, \tag{A.14}$$

which proves the statement that the system is in the unitary state $|u_i\rangle$ except for a global phase $e^{i\theta} = \langle u_i|\psi(t)\rangle/|\langle u_i|\psi(t)\rangle|$, according to Eq. (A.12). Also note that $p(\lambda_i|t) = |\langle u_i|\psi(t)\rangle|^2 = \langle\psi(t)|\mathbf{P_i}|\psi(t)\rangle$.

But what happens when the eigenvalue λ_i is degenerate? In this case, there is a subspace g of $\mathbf{O}$ associated with λ_i and the projector $\mathbf{P_i}$ is given by $\sum_{g=1}^{k}|u_i^g\rangle\langle u_i^g|$, where k is the number of degeneracies associated with this eigenvalue. Consequently, Eq. (A.12) is expressed as

$$\frac{\mathbf{P_i}\,|\psi(t)\rangle}{\sqrt{\langle\psi(t)|\mathbf{P_i}|\psi(t)\rangle}} = \frac{(\sum_{g=1}^{k}|u_i^g\rangle\langle u_i^g|)|\psi(t)\rangle}{\sqrt{\sum_{g=1}^{k}\langle\psi(t)|u_i^g\rangle\langle u_i^g|\psi(t)\rangle}} = \frac{\sum_{g=1}^{k}\langle u_i^g|\psi(t)\rangle|u_i^g\rangle}{\sqrt{\sum_{g=1}^{k}|\langle u_i^g|\psi(t)\rangle|^2}}, \tag{A.15}$$

and the new system will be a unit vector formed by the combination of states proportional to $|u_i^g\rangle$.

Note in Eq. (A.15) that the probability of the system collapsing for $|u_i^g\rangle$ is given by $p(\lambda_i|t) = \langle\psi(t)|\mathbf{P_i}|\psi(t)\rangle = \sum_{g=1}^{k}|\langle u_i^g|\psi(t)\rangle|^2$. Since

$$\mathbf{O} = \begin{bmatrix}\lambda_{11} & \cdots & 0\\ \vdots & \ddots & \vdots\\ 0 & \cdots & \lambda_{NN}\end{bmatrix} = \sum_{i=1}^{N}\sum_{g=1}^{k}\lambda_i|u_i^g\rangle\langle u_i^g|, \tag{A.16}$$

Eq. (A.16) can be used to calculate the expected value $\langle\mathbf{O}\rangle$ over all possible results from the measurement of the operator $\mathbf{O}$ on the state$|\psi(t)\rangle$ [34], as

$$\langle\mathbf{O}\rangle = \sum_{i=1}^{N}\lambda_i\,p(\lambda_i|t) = \sum_{i=1}^{N}\lambda_i\,\langle\psi(t)|\mathbf{P_i}|\psi(t)\rangle = \tag{A.17}$$

$$\sum_{i=1}^{N}\lambda_i\,\langle\psi(t)|(\sum_{g=1}^{k}|u_i^g\rangle\langle u_i^g|)|\psi(t)\rangle =$$

$$\langle\psi(t)|(\sum_{i=1}^{N}\sum_{g=1}^{k}\lambda_i|u_i^g\rangle\langle u_i^g|)\,|\psi(t)\rangle = \langle\psi(t)|\mathbf{O}|\psi(t)\rangle.$$

The average provided by Eq. (A.17) can be calculated directly through an inner product between $\mathbf{O}|\psi(t)\rangle$ and $\langle\psi(t)|$, where the latter is the dual vector of the wave function presented in Eq. (4). In parallel, this prediction can be verified experimentally by a sequence of measurements on identical systems prepared under similar conditions, after counting the results λ_i and their respective frequency of occurrence (which should be close to $p(\lambda_i|t)$). This is the essence of most of *Pennylane* algorithms [59], where the expected value of a specific

observable is calculated after the outputs of the quantum circuit are measured and the results are recorded based on a certain number of “shots”.

Appendix B: Mathematical Example of Encoding Statistical Data into Quantum States

In this appendix, we will demonstrate how a classical statistical feature extracted from a signal (i.e., the mean value), can be transformed into a quantum state using quantum embedding techniques. We will use **angular encoding** for this handmade example and show how the same data could be encoded into quantum states for 1, 2, and 3-qubits systems.

Extracting the Classical Data x

Assume that after collecting the acceleration signals from a structure, the mean acceleration value extracted following the *min-max* normalization process (within a range of [0,1]) is 0.6. Thus:

$$x = 0.6 \tag{B.1}$$

1) Encoding for 1-Qubit

To encode x into a quantum state, we apply a rotation gate $\mathbf{R_z(\theta)}$, where the rotation is $\theta = 2\pi x$. Thus, the normalized range [0,1] spans 360° of an axis of the Bloch sphere. For $x = 0.6$, we have:

$$\theta = 2\pi \times 0.6 = 1.2\pi \tag{B.2}$$

The rotation operation over the *z*-axis is represented by the matrix:

$$\mathbf{R_z(\theta)} = \begin{pmatrix} \cos(\theta/2) & -i\,sin(\theta/2) \\ -i\,sin(\theta/2) & \cos(\theta/2) \end{pmatrix} \tag{B.3}$$

The following calculations are approximated to three decimal places for better understanding. Substituting $\theta = 1.2\pi$, we get:

$$\mathbf{R_z}(1.2\pi) = \begin{pmatrix} \cos(0.6\pi) & -i\,sin(0.6\pi) \\ -i\,sin(0.6\pi) & \cos(0.6\pi) \end{pmatrix} \approx \begin{pmatrix} -0.309 & -0.951i \\ -0.951i & -0.309 \end{pmatrix} \tag{B.4}$$

Now, we apply this rotation to the basis state $|0\rangle$:

$$|x\rangle = \mathbf{R_z}(1.2\pi)|0\rangle = \begin{pmatrix} -0.309 & -0.951i \\ -0.951i & -0.309 \end{pmatrix}\begin{pmatrix} 1 \\ 0 \end{pmatrix} = \begin{pmatrix} -0.309 \\ -0.951i \end{pmatrix} \tag{B.5}$$

Thus, the resulting quantum state is:

$$|x\rangle = -0.309|0\rangle - 0.951i|1\rangle \tag{A.6}$$

This state represents the classical data $x = 0.6$ encoded as a quantum state. Additionally, the probabilities of measuring $|0\rangle$ and $|1\rangle$ are:

$$P(0) = |-0.309|^2 \approx 0.095 \quad \text{(B.7)}$$
$$P(1) = |-0.951i|^2 \approx 0.904$$

Note that the sum of probabilities of the quantum states is equal to 1.

2) Encoding for 2-Qubits

To encode the same data into a quantum state with 2 qubits, we apply the rotation $R_z(1.2\pi)$ to each qubit separately. The total operation is the tensor product (symbol $\otimes$) of two rotations:

$$\mathbf{U} = \mathbf{R_z}(1.2\pi) \otimes \mathbf{R_z}(1.2\pi) \quad \text{(B.8)}$$

Starting with the initial state $|00\rangle$, we apply the operation:

$$|x_2\rangle = \mathbf{R_z}(1.2\pi) \otimes \mathbf{R_z}(1.2\pi)|00\rangle \quad \text{(B.9)}$$

Using the matrix for $\mathbf{R_z}(1.2\pi)$, we get:

$$|x_2\rangle = \begin{pmatrix} -0.309 \\ -0.951i \end{pmatrix} \otimes \begin{pmatrix} -0.309 \\ -0.951i \end{pmatrix} \quad \text{(B.10)}$$

Expanding Eq. (B.10), we get:

$$|x_2\rangle = 0.095|00\rangle + 0.294i|01\rangle + 0.294i|10\rangle + 0.904|11\rangle \quad \text{(B.11)}$$

This is the quantum state for the 2-qubit system. Additionally, the probabilities of measuring $|00\rangle$, $|01\rangle$, $|10\rangle$ and $|11\rangle$ are:

$$P(00) = |0.095|^2 \approx 0.009$$
$$P(01) = |0.294i|^2 \approx 0.086$$
$$P(10) = |0.294i|^2 \approx 0.086 \quad \text{(B.12)}$$
$$P(11) = |0.904|^2 \approx 0.817$$

3) Encoding for 3-Qubits

Finally, for a 3-qubit system, we apply the same rotation $\mathbf{R_z(1.2\pi)}$ to each of the three qubits. The total operation is the tensor product of three rotations:

$$\mathbf{U} = \mathbf{R_z}(1.2\pi) \otimes \mathbf{R_z}(1.2\pi) \otimes \mathbf{R_z}(1.2\pi) \tag{B.13}$$

Next, we apply the unitary operation $\boldsymbol{U}$ to the initial state of the system $|000\rangle$:

$$|x_3\rangle = \mathbf{R_z}(1.2\pi) \otimes \mathbf{R_z}(1.2\pi) \otimes \mathbf{R_z}(1.2\pi)|000\rangle \tag{B.14}$$

Using the matrix for $R_z(1.2\pi)$, we get:

$$|x_3\rangle = \begin{pmatrix} -0.309 \\ -0.951i \end{pmatrix} \otimes \begin{pmatrix} -0.309 \\ -0.951i \end{pmatrix} \otimes \begin{pmatrix} -0.309 \\ -0.951i \end{pmatrix} \tag{B.15}$$

The result is a superposition of all eight possible states for the 3-qubit system:

$$\begin{aligned} |x_3\rangle = {} & -0.030|000\rangle - 0.091i|001\rangle - 0.091i|010\rangle + 0.280|011\rangle \\ & - 0.091i|100\rangle + 0.280|101\rangle + 0.280|110\rangle + 0.860i|111\rangle \end{aligned} \tag{B.16}$$

This is the quantum state for the 3-qubit system, representing the classical data encoded into a superposition of quantum states. Additionally, the probabilities of measuring states $|000\rangle$, $|001\rangle$, $|010\rangle$, $|011\rangle$, $|100\rangle$, $|101\rangle$, $|110\rangle$ and $|111\rangle$ are:

$$\begin{aligned} P(000) &= |-0.030|^2 \approx 0.001 \\ P(001) &= |-0.091i|^2 \approx 0.008 \\ P(010) &= |-0.091i|^2 \approx 0.008 \\ P(011) &= |0.280|^2 \approx 0.0784 \\ P(100) &= |-0.091i|^2 \approx 0.008 \\ P(101) &= |0.280|^2 \approx 0.078 \\ P(110) &= |0.280|^2 \approx 0.078 \\ P(111) &= |0.860i|^2 \approx 0.740 \end{aligned} \tag{B.17}$$

Next operations:

After the quantum embedding process, the next step is to apply the following set of operations to the encoded quantum states, described by the unitary operator $\mathbf{V(\alpha, \gamma)}$, which has trainable parameters. This operator consists of a series of quantum gates, i.e., a set of specific tensor product matrices, just like the calculations performed earlier: $\mathbf{V(\alpha, \gamma)} \otimes \mathbf{U} \otimes |00 \ldots 0\rangle = \mathbf{V(\alpha, \gamma)} \otimes |\mathrm{x}\rangle$.

Appendix C: Unsupervised QML Pseudocodes

A pseudocode is introduced to ease reproducibility and better understanding of the version of QVR algorithm used in this study, which is adapted from [45]. The procedure consists of two steps: unsupervised training (Pseudocode A) and testing (Pseudocode B). For variables that are not specified below, please refer to the paper.

Pseudocode A: Unsupervised training phase

Input: A set of T-many features classical data $\boldsymbol{x^{normal}} = (\boldsymbol{x_t}: t \in T)$ extracted from normal/intact acceleration signal samples, optimization routine, EPOCH, EXP denotes $\{1, 2, \ldots, NE\}$ the number of terms NE used in the calculation of the cost function, a penalty function P, two Ansätze circuits $\boldsymbol{U}$ and $\boldsymbol{W}$.

Set initial values for the parameters $\boldsymbol{\theta} = [\boldsymbol{\alpha}, \boldsymbol{\mu}, \boldsymbol{\sigma}]$.
for $j = 1$ to EPOCH **do**
Choose random batches $B_X \subseteq X$ and $B_T \subseteq \{t_1, \ldots, t_p\}$
for $i = 1$ to B_X **do**
for k in EXP **do**
Choose a diagonal matrix $M(\boldsymbol{\gamma})$ with eigenvalues $\boldsymbol{\gamma}$ chosen uniformly randomly with $\boldsymbol{\gamma} \sim (\mu_s, \sigma_s)$
for t_j in B_T **do**
Prepare the state embedding circuit $\boldsymbol{U}[\boldsymbol{x}_i(t_j)]$ (Method: angle encoding)
Prepare the state $|\boldsymbol{x}_i(t_j)\rangle \coloneqq \boldsymbol{U}[\boldsymbol{x}_i(t_j)]|0\rangle^{\otimes n}$ with n qubits
Prepare the circuit $\boldsymbol{W}^{\dagger}(\boldsymbol{\alpha})D(\boldsymbol{\gamma}, t_j)\boldsymbol{W}(\boldsymbol{\alpha})$
Prepare the state $|\boldsymbol{x}_i(t_j), \boldsymbol{\theta}\rangle \coloneqq \boldsymbol{W}^{\dagger}(\boldsymbol{\alpha})D(\boldsymbol{\gamma}, t_j)\boldsymbol{W}(\boldsymbol{\alpha})|\boldsymbol{x}_i(t_j)\rangle$
Compute the single point cost $\Omega(\boldsymbol{x}_i(t_j), \boldsymbol{\alpha}, \boldsymbol{\gamma})$
end for
Compute an instance of the single time series cost function $C_2(\boldsymbol{x}_i, \theta)^- \coloneqq \frac{1}{N_T}\sum_{t_j} \Omega^2(\boldsymbol{x}_i(t_j), \boldsymbol{\alpha}, \boldsymbol{\gamma})$
using $\boldsymbol{\theta} = [\boldsymbol{\alpha}, \boldsymbol{\mu}, \boldsymbol{\sigma}]$
end for
Compute the intermediate cost function $C_2(\boldsymbol{x}_i, \boldsymbol{\theta}) = E_{\boldsymbol{\gamma} \sim N(\mu_s, \sigma_s)}[C_2(\boldsymbol{x}_i, \boldsymbol{\theta})^-]$
end for
Compute the final cost function $C(\boldsymbol{\theta}) \coloneqq \frac{1}{2N_X}\sum_{\boldsymbol{x}_i \in B_X} C_2(\boldsymbol{x}_i, \theta) + P_\tau(\boldsymbol{\sigma})$
Run next step of the classical optimization routine
Update the parameters $\boldsymbol{\theta} = [\boldsymbol{\alpha}, \boldsymbol{\mu}, \boldsymbol{\sigma}]$
end for

Output: The optimized parameters $\boldsymbol{\theta}^* = [\boldsymbol{\alpha}^*, \boldsymbol{\mu}^*, \boldsymbol{\sigma}^*]$ and the cost $C(\boldsymbol{\theta}^*)$.

Pseudocode B: Classification Phase

Input: A set of T-many features classical data $\boldsymbol{x^{unknown}} = (\boldsymbol{x_t}: t \in T)$ extracted from unknown acceleration signal samples, the optimized parameters $\boldsymbol{\theta}^* = [\boldsymbol{\alpha}^*, \boldsymbol{\mu}^*, \boldsymbol{\sigma}^*]$, Ansätze circuits $\boldsymbol{U}$ and $\boldsymbol{W}$ chosen in the training phase and the penalty function P chosen in the training phase.

for k in EXP **do**

Choose a diagonal matrix $M(\boldsymbol{\gamma})$ with eigenvalues $\boldsymbol{\gamma}$ chosen uniformly randomly with $\boldsymbol{\gamma} \sim (\mu_s^*, \sigma_s^*)$

for t_j in B_T **do**

Prepare the state embedding circuit $\boldsymbol{U}[\boldsymbol{x}_i(t_j)]$ (Method: angle encoding)

Prepare the state $|\boldsymbol{x}_i(t_j)\rangle \coloneqq \boldsymbol{U}[\boldsymbol{x}_i(t_j)]|0\rangle^{\otimes n}$ with n qubits

Prepare the circuit $\boldsymbol{W}^{\dagger}(\boldsymbol{\alpha}^*)D(\boldsymbol{\gamma}, t_j)\boldsymbol{W}(\boldsymbol{\alpha}^*)$

Prepare the state $|\boldsymbol{x}_i(t_j), \boldsymbol{\theta}^*\rangle \coloneqq \boldsymbol{W}^{\dagger}(\boldsymbol{\alpha}^*)D(\boldsymbol{\gamma}, t_j)\boldsymbol{W}(\boldsymbol{\alpha}^*)|\boldsymbol{x}_i(t_j)\rangle$

Compute the single point cost $\Omega(\boldsymbol{x}_i(t_j), \boldsymbol{\alpha}^*, \boldsymbol{\gamma}^*)$

end for

Compute an instance of the single time series cost function $C_2(\boldsymbol{x}_i, \boldsymbol{\theta}^*)^- \coloneqq \frac{1}{N_T}\sum_{t_j} \Omega^2(\boldsymbol{x}_i(t_j), \boldsymbol{\alpha}^*, \boldsymbol{\gamma}^*) + P_\tau(\boldsymbol{\sigma})$

end for

Compute the single cost function $C_2(\boldsymbol{x}_i, \boldsymbol{\theta}^*) = E_{\boldsymbol{\gamma} \sim N(\mu_s, \sigma_s)}[C_2(\boldsymbol{x}_i, \boldsymbol{\theta}^*)^-]$

Output: $a_{\boldsymbol{x^{normal}}}(x^{unknown}) \coloneqq [2C(\boldsymbol{\theta}^*) - 2P_\tau(\boldsymbol{\sigma}) - C_2(\boldsymbol{x}_i, \boldsymbol{\theta}^*)]$

Appendix D: List of customizable parts of QML

The QVR's algorithm editable elements are listed in Table I with their respective explanations.

Elements	Explanation and connection to other QVR components
n	Number of qubits used in the system.
$\boldsymbol{x^{normal}}$ and $\boldsymbol{x^{unknown}}$	Set of normal and unknown features, respectively. This can be chosen to be any set of features extracted from the acceleration signal samples.
$\mathbf{W(\alpha)}$	Parameterized unitary used in the eigendecomposition of $e^{-iH(\boldsymbol{\alpha},\boldsymbol{\gamma})}$ where $\boldsymbol{\alpha}$ and $\boldsymbol{\gamma}$ are vectors of free parameters. $\boldsymbol{\gamma}$ is sampled from $N(\boldsymbol{\mu},\boldsymbol{\sigma})$ where $\boldsymbol{\mu}$ and $\boldsymbol{\sigma}$ are also free parameters of the model. This can be chosen to be any parameterized quantum circuit.
$\mathbf{D(\gamma, t_j)}$	Parameterized diagonal unitary used in the eigendecomposition of $e^{-iH(\boldsymbol{\alpha},\boldsymbol{\gamma})}$. This can be chosen to be any parameterized quantum circuit implementation of a diagonal unitary
$\mathrm{U[x_i(t_j)]}$	Unitary employed to encode a set of classical data vector $\boldsymbol{x_i}$ at feature t_j into a quantum state $\lvert \boldsymbol{x}_i(t_j)\rangle$. This is commonly known as a "quantum feature map".
$\mathbf{P_\tau(\sigma)}$	A penalty function for large inputs in the parameter vector σ, where τ is a hyperparameter vector. The penalty can be implemented using any sigmoidal function.
Classical Optimizer	A classical computer procedure for calculating $\boldsymbol{\theta}^*$. Performance of the optimization depends on (I) the starting parameters $\boldsymbol{\theta_{init}}$, (II) the feature set size, (III) the mini-batch size, and (IV) the convergence criterion.
EPOCH	The number of iterations of training taken to optimize $\boldsymbol{\theta}^*$**.** This often defines a computational time/precision trade-off.

Table I - The customizable elements of QVR.

4 FINAL CONSIDERATIONS

The study presented in this dissertation is a pioneering effort in investigating the use of unsupervised QML for SHM. It is intended to serve as a base for further research on the subject as well as a benchmark for comparing other quantum methods. Although designed as an initial approach, the methodology was validated on both laboratory and real-world structures, specifically a two-story frame and a full-scale railway bridge, respectively. The strategy employs eleven statistical features extracted from acceleration signals, which are embedded into quantum states and subsequently fed into a quantum circuit. The training phase is conducted exclusively using healthy data, and an anomaly score function is calibrated to highlight deviations from the structure's standard dynamic response. This approach enables the detection of structural abnormalities through an unsupervised procedure. The technique developed in this dissertation yielded encouraging outcomes in the detection, localization and quantification of damage during the conducted trials.

Finally, the quantum technique demonstrated comparable or superior performance to classical clustering methods (such as k-means and hierarchical clustering), indicating its relevance for SHM applications. The specific results, along with suggestions for future studies, are detailed in the chapter “Concluding Remarks and Future Work” of the paper. The science of Quantum Computing is still in its early stages, and broader adoption would require significant advancements in infrastructure and hardware development. However, with technological progress and scalability, this approach could eventually surpass the well-stablished classical ML in certain applications.

This work represents an important step toward integrating QML into SHM, showing its potential to address current challenges and inspire new solutions to monitor and protect structures, enhancing their safety and resilience. Furthermore, the concepts and techniques covered in this study can encourage the search for innovative applications and ideas in other research fields.

5 PUBLISHED WORKS RELATED TO THE TOPIC

The paper resulting from this dissertation can be referenced as:

- **ALVES, V.**; GOMES, R.; CURY, A. New Perspectives on Structural Health Monitoring using Unsupervised Quantum Machine Learning. *Mechanical Systems and Signal Processing*, v. 229, p. 112489, 2025.

The initial stages of this research were presented during the author's undergraduate studies at the "XXVIII UFJF Scientific Initiation Seminar" in 2023, which received an honorable mention award in the Exact Sciences category. The presentation's GitHub can be accessed at: https://github.com/Victor-Higino-Meneguitte-Alves/SEMIC2023_QuantumML.git.

- **ALVES, V.**; GOMES, R.; CURY, A. Detecção de Danos em Estruturas via Aprendizado de Máquina Quântico. *29° Seminário de Iniciação Científica da UFJF - XXIX SEMIC*. 2023. (Work Presentation/Seminar).

In addition, other articles published by the author over four years of scientific initiation in the Department of Applied and Computational Mechanics at the Federal University of Juiz de Fora (UFJF) within the SHM research line, including those in journals, conferences, and book chapters, are listed.

Journals:

- KAUSS, K.; **ALVES, V.**; BARBOSA, F.; CURY, A. Semi-supervised structural damage assessment via autoregressive models and evolutionary optimization. *Structures*. Elsevier, p. 105762, 2024.
- **ALVES, V.**; CURY, A. An automated vibration-based structural damage localization strategy using filter-type feature selection. *Mechanical Systems and Signal Processing*, v. 190, p. 110145, 2023.
- **ALVES, V.**; ALVES, V.; CURY, A. Monitoramento de integridade estrutural utilizando inteligência artificial: Desafios, avanços e aplicações. *Revista da UFMG*, v. 30, 2023.
- **ALVES, V.**; CURY, A. A fast and efficient feature extraction methodology for structural damage localization based on raw acceleration measurements. *Structural Control and Health Monitoring*, v. 28, n. 7, p. e2748, 2021.

Book Chapter:

- **ALVES, V.**; ALVES, V.; CURY, A. Artificial Intelligence-Driven Structural Health Monitoring: Challenges, Progress, and Applications. In: *New Advances in Soft Computing in Civil Engineering: AI-Based Optimization and Prediction*. Cham: Springer Nature Switzerland, p. 149-166, 2024.

Conferences:

- **ALVES, V.**; CURY, A. Unsupervised feature selection-based technique for locating structural deterioration: a multi-domain approach. In: XLIII Ibero-Latin American Congress on Computational Methods in Engineering, 2022, Foz do Iguaçu. *Proceedings of the XLIII CILAMCE, 2022.*
- **ALVES, V.**; BARBOSA, F.; CURY, A. A data-driven feature selection-based procedure for automatic bridge damage localization. In: I Latin-American Workshop on Structural Health Monitoring, 2023, Cartagena, Colômbia. *Proceedings of the I LATAM-SHM, 2023.*